Urban Climate 47 (2023) 101359

Contents lists available at ScienceDirect

Urban Climate

journal homepage: www.elsevier.com/locate/uclim

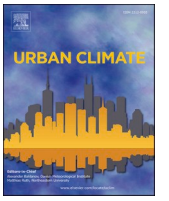

Modelling long-term thermal comfort conditions in urban environments using a deep convolutional encoder-decoder as a computational shortcut

Ferdinand Briegel [a,*], Osama Makansi [b], Thomas Brox [b], Andreas Matzarakis [a,c], Andreas Christen [a]

[a] Chair of Environmental Meteorology, Faculty of Environment and Natural Resources, University of Freiburg, Freiburg im Breisgau, Germany
[b] Department of Computer Science, University of Freiburg, Freiburg im Breisgau, Germany
[c] Research Centre Human Biometeorology, German Meteorological Service, Freiburg im Breisgau, Germany

ARTICLE INFO

Keywords:
CNN
U-Net
SOLWEIG
Mean radiant temperature (T_{mrt})
Urban thermal comfort
Urban climate informatics

ABSTRACT

Different urban microscale models exist to model street-level mean radiation temperature (T_{mrt}). However, these models are computationally expensive, albeit to varying degrees. We present a computational shortcut using a convolutional encoder-decoder network (U-Net) to predict pedestrian level (1.1 m a.g.l.) T_{mrt} at a building-resolved scale (1 × 1 m). SOLWEIG is used to create spatial training data for 68 days at hourly resolution in the city of Freiburg, Germany. Validation of the model was carried out in two steps: First, SOLWEIG (and U-Net) were validated against T_{mrt} point measurements. Second, U-Net was validated against SOLWEIG on 6 areas and 12 days resulting in a MAE of 2.4 K. The U-Net is 22 times faster than SOLWEIG, and thus able to emulate a micrometeorological physical model with computational superiority. As a demonstration case, U-Net is applied to model T_{mrt} for the urbanized area of Freiburg for two complete 30-year periods (1961–1990, 1991–2020) driven by hourly ERA5-Land reanalysis data. Summertime daily maximum T_{mrt} increased on average by 2.5 K, whereas summertime daily maximum air temperature increased by only 1.5 *K*. Maximum T_{mrt} increase is stronger on non-tree covered paved areas (2.8 K) than on tree covered grassy areas (1.8 K).

1. Introduction

Average heat-related mortality per year increased by almost 54% globally from 2000–2004 to 2014–2018 for people over 65 (Watts et al., 2021). Furthermore, heat waves account for the most fatalities of extreme weather events in Europe (EEA, 2017). According to the Synthesis Report of the Intergovernmental Panel on Climate Change (IPCC), global air temperature (T_a) will increase in the future due to global climate change (Seneviratne et al., 2021). In turn, the increase of global T_a will favour heat wave events at the same time (Bindoff et al., 2013; Seneviratne et al., 2021). The physical characteristics of urban areas make them more vulnerable to extreme weather events, such as heat waves, than rural areas. (Oke et al., 2017). In urban areas, buildings' geometry, thermal and radiative properties and vegetation cover differ from those in rural areas, resulting in generally elevated T_a, referred to as Urban Heat Island – UHI (Oke et al., 2017).

* Corresponding author at: Werthmannstraße 12, 79100 Freiburg, Germany.
E-mail address: ferdinand.briegel@meteo.uni-freiburg.de (F. Briegel).

https://doi.org/10.1016/j.uclim.2022.101359
Received 29 June 2022; Received in revised form 16 October 2022; Accepted 17 November 2022
Available online 13 December 2022

Li and Bou-Zeid (2013) investigated the relationship between heat waves and UHI and found that heat stress in cities during heat waves is higher than the sum of a background UHI and the heat wave effect alone. These findings indicate that urban areas are more exposed to increasing thermal stress than rural areas due to climate change. As heat waves become more frequent in the future and the global urban population is expected to increase (United Nations, 2019), the proportion of people exposed to heat stress will increase tremendously (Li and Bou-Zeid, 2013). This illustrates how intensely human thermal comfort and, thus, well-being depends on adaption to heat waves and UHI in cities (Bindoff et al., 2013).

Different thermal indices can express human thermal comfort (VDI, 2008). Thermal indices have been developed to link environmental and physiological (based on human energy balance) variables to describe better thermal comfort / total heat stress of an individual (Epstein and Moran, 2006; Potchter et al., 2018; Staiger et al., 2019). Several studies concluded that mean radiation temperature (T_{mrt}) is the driving parameter of outdoor human thermal comfort during daytime (Holst and Mayer, 2011; Kántor and Unger, 2011; Cohen et al., 2012). In addition to topographic conditions, the complex and heterogeneous three-dimensional structures of cities cause high spatial and temporal variability of T_{mrt} and other relevant environmental variables for calculating thermal indices. Of these environmental variables, T_{mrt} and wind have the highest variability on the microscale (Matzarakis et al., 2016). This has the consequence that T_{mrt} and wind have to be modelled at building-resolving scale when assessing current and future heat stress exposure in urban outdoor spaces.

Various microscale (building-resolving) models exist to model T_{mrt} in urban settings:

ENVI-met (Bruse, 1999), SkyHelios / RayMan (Matzarakis et al., 2007, 2010; Fröhlich and Matzarakis, 2018), and SOLWEIG (Lindberg et al., 2008) are common models to predict T_{mrt} in complex building-resolved urban contexts. These models differ in their underlying physical properties, but their output have been validated / intercompared in several studies (Chen et al., 2014; Szűcs et al., 2014; Jänicke et al., 2015; Kántor et al., 2018; Gál and Kántor, 2020; Liu et al., 2020). However, these models have one downside in common: they are computationally expensive, albeit to varying degrees. This means study area and time might be very limited depending on spatial and temporal resolution. While this is sufficient for case studies where micro-level processes are modelled for different neighbourhoods in limited periods, accurate micro-level calculations over long periods or entire cities are not possible (e.g., downscaling global climate projections over decades or calculating building resolved human thermal comfort for entire cities with e.g., 10 × 10 km domain size). Thus, it would be helpful to have a fast and accurate model to project future urban climate conditions over long periods while retaining the required building-resolved information and possibly taking different climate change projections and urban development scenarios into account.

Machine learning and deep learning methods became an important part of urban climate informatics (Middel et al., 2022) and gained more attention for modelling urban climate, while overcoming the computational drawbacks of physical models: Support Vector Machines were used to model T_a for courtyards (Diz-Mellado et al., 2021), regressions and gradient boosted trees to model T_{mrt} / radiation on building-resolved scale (Ketterer and Matzarakis, 2016; Vartholomaios, 2019), and feedforward Multi-Layer Perceptron (MLP) approaches to model building-resolved T_{mrt} (Xie et al., 2022), pointwise T_a (Oh et al., 2020), or thermal comfort (Kariminia et al., 2016; Chan and Chau, 2019). The mentioned examples use different methods to receive the corresponding predictors and response data. Ketterer and Matzarakis (2016), for example, used the RayMan model (Fröhlich and Matzarakis, 2018) to simulate PET and T_{mrt} as response data and used measurement data as predictors, while Chan and Chau (2019) used data from field questionnaire surveys on outdoor thermal comfort and field measurements to train an ANN for thermal comfort prediction in urban parks. The mentioned studies partly used benchmark models which were outperformed by ANNs (liner model in Ketterer and Matzarakis (2016); ARIMA model in Oh et al. (2020), RayMan in Chan and Chau (2019), and T_{mrt} obtained by surface T (Xie et al., 2022)). While MLPs have already been successfully applied in urban meteorology, more complex deep learning architectures have not yet been used. However, convolutional neural networks (CNN) and recurrent neural networks (RNN) have been successfully used in other, non-urban, meteorological subfields. A combination of CNN and Long-Short-Term-Memory (LSTM) layers was successfully applied to forecast short-term pointwise T_a (Kreuzer et al., 2020; Jeong et al., 2021) and to forecast T_a for a 36 × 36 grid covering China (Zhang and Dong, 2020). The used MLP and CNN models, however, were applied to solve a regression problem for one point in which no spatial relationships between neighbouring grid cells were considered.

Spatial relationships can be considered by fully convolutional networks (FCN) and U-Nets (a special type of FCN – Ronneberger et al. (2015)), as they allow image to image processing and therefore have the advantage of learning spatial patterns of the training data (see appendix A). This means U-Nets are more capable of mapping varying temporal and spatial predictors in space. U-Nets were first used for biomedical image segmentation and needed fewer training data than comparable architectures (Ronneberger et al., 2015). Different FCN types, auto-encoders, and U-Net architectures have recently been used for now- and forecast meteorological variables at the synoptic scale in weather forecasting applications (Larraondo et al., 2019; Weyn et al., 2019, 2020; Trebing et al., 2021) and climate modelling (Sha et al., 2020).

This study presents a U-Net approach for modelling T_{mrt} at the microscale in complex urban areas. To the authors' knowledge, U-Net-like architectures have not yet been used for modelling T_{mrt}. Training a neural network requires representational training and test data. We use SOLWEIG to model T_{mrt} (at 1.1 m a.g.l.) for 62 areas (500 × 500 m) and on 80 days (hourly resolution) as response data. The spatial and temporal inputs of SOLWEIG are, in turn, used as input features for the U-Net. In addition, data from a T_{mrt} measurement campaign is used to validate SOLWEIG and U-Net. To demonstrate a potential application, the trained U-Net is then applied to model long-term (60 years at hourly resolution) T_{mrt} for an area with a 500 × 500 m extent at a resolution of 1 m for the City centre of Freiburg, Germany. For that purpose, ERA5-Land hourly data are used from 1960 to 2020.

The following objectives are addressed in this study: 1. U-Net is able to generalize and model T_{mrt} on unknown areas and weather situations accurately; 2. U-Net is computational fast with a positive trade-off between predictive uncertainty and computational speed; and 3. U-Net allows for computationally efficient long-term modelling of spatially distributed T_{mrt} in urban areas.

2. Methods

This chapter describes how spatial and temporal predictors are created, how training and test areas are sampled, how physical model simulations are conducted, how the architecture and training process of the U-Net is set-up, and how the U-Net is validated.

2.1. Study area

The study area covers the city of Freiburg im Breisgau (48°00′ N, 07°51′ E). Freiburg is located in southwestern Germany (Baden-Württemberg), at the transition from the Upper Rhine Valley to the Black Forest (Fig. 1). In recent years, the Upper Rhine Valley has become more exposed to droughts and heat waves.

2.2. Data

Section 2.2 describes the collection of validation data (2.2.1 Validation Data), the pre-processing of spatial and temporal data to obtain spatial and temporal predictors (2.2.2 Spatial and temporal predictors) and the sampling of training and test data (2.2.3 Sampling of training and test data).

2.2.1. Validation data

Point measurements were collected within the city of Freiburg in field campaigns within the KLIMES project (Mayer, 2008). On individual days between January 2007 and August 2008, T_a, vapour pressure, wind speed, short-, and long-wave radiation were continuously recorded at selected locations representing different urban structures (Holst and Mayer, 2011). T_{mrt} values were derived from short- and long-wave radiant flux densities measured by the six-directional method at 1.1 m a.g.l (Mayer et al., 2008). For a detailed description of the measurement campaign see Mayer et al. (2008) and Holst and Mayer (2011). This study uses stationary measurements from 12 individual days, with 3 sites including measurements throughout the night (Table 1). Measurement data has a temporal resolution of 10 min.

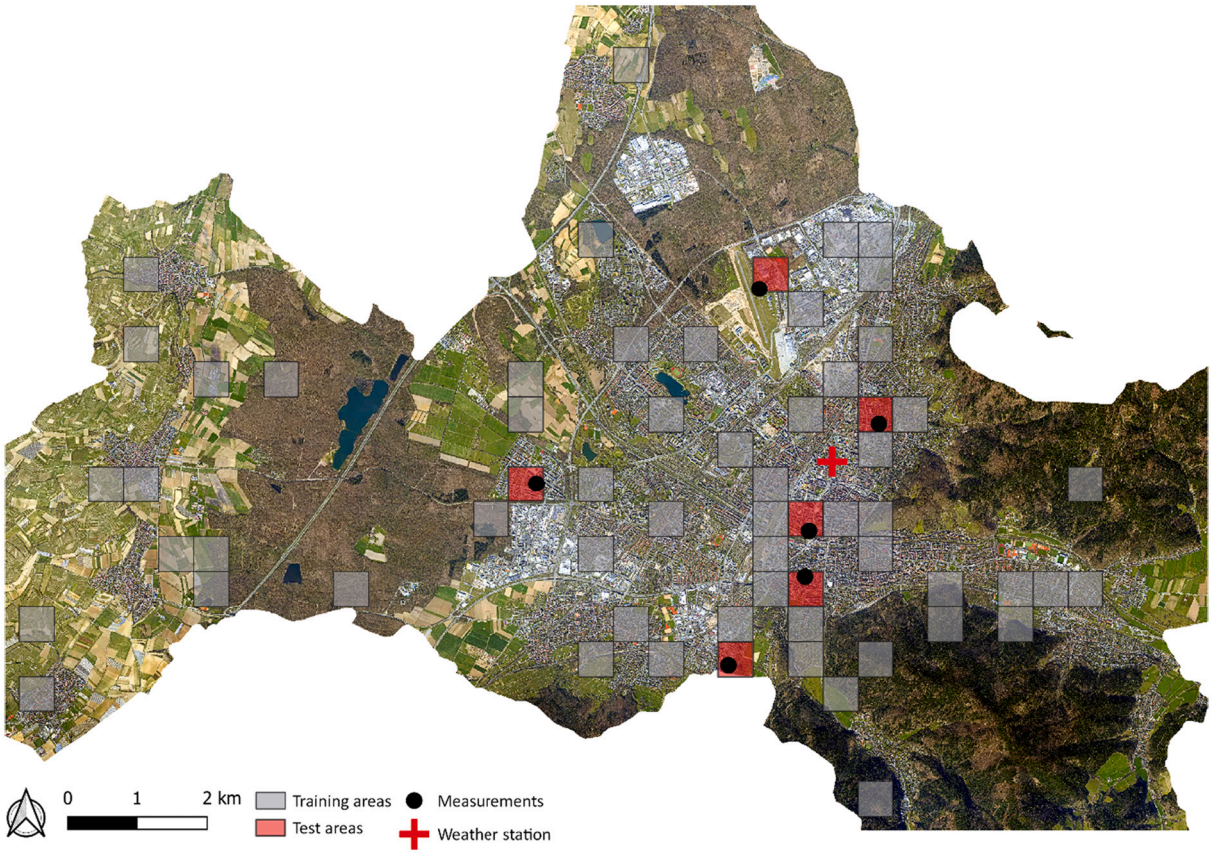

Fig. 1. Administrative boundary of Freiburg with training areas (grey) and test areas (red). Red cross indicates location of an urban weather station, black dots represent locations of the measurement campaign in 2007 / 2008 (KLIMES). Data basis of orthophoto: City of Freiburg (Freiburg, 2019). (For interpretation of the references to color in this figure legend, the reader is referred to the web version of this article.)

2.2.2. Spatial and temporal predictors

Both SOLWEIG and U-Net need spatial (geometric) and temporal (meteorological) input data. All spatial data has a resolution of 1 m. A digital elevation model (DEM) is derived from LIDAR (Freiburg, 2021). In addition, LIDAR and building outline data (derived from CityGML with level of detail 1 – Freiburg, 2018) are used to obtain a digital surface model containing ground and building heights (DSMb) and a digital surface model containing vegetation heights above ground and zero values for pixels not covered by vegetation (DSMv). SOLWEIG requires land cover classes of buildings, paved surfaces, grass, water and bare soil. A land cover class map is created by clipping different OpenStreetMap layers (OSM, 2017) and Copernicus Urban Atlas data (EEA, 2018). Gaps in the land cover class map are filled by a Support Vector Machine (SVM) trained on about 10,000 points using the channels of an RGB orthophoto (Freiburg, 2019) as predictors. The SVM is set up with a radial basis kernel and has a mean misclassification error of <10%.

Besides land cover and digital surface models SOLWEIG requires sky view factor maps (SVF) and shadow matrices. Both SVF and shadow matrices are calculated by the Urban Multi-scale Environmental Predictor (UMEP - Lindberg et al., 2018) using the anisotropic model (Wallenberg et al., 2020) with digital building and vegetation surface models. The anisotropic model divides the sky vault for each 1 × 1 m position into 145 patches with the value 0 for obstructed and 1 for an unobstructed view resulting in 145 shadow matrices. Model parameters transmissivity of light through vegetation and trunk height are default (Table 3). SVF and shadow matrices of all areas are calculated by applying an extra buffer of 100 m around the training / test areas to prevent edge effects. 15 SVF maps are calculated, representing the different cardinal directions and building / vegetation combinations (see Lindberg et al., 2018). UMEP is also used to calculate wall aspect and wall height raster maps. In sum, the U-Net is trained on 21 spatial predictors: DEM, DSMb, DSMv, land cover classes, wall aspect, wall height, and the 15 SVF maps. SOLWEIG uses additionally the 145 shadow matrices. Fig. S1 shows spatial data examples for DEM, DSMb, DSMv, land cover, SVF, and wall height.

Meteorological input data is provided by an urban weather station located in the northern part of the city (48° 00′ 04“ N, 7° 50’ 55” E; red cross in Fig. 1). The station is placed on a rooftop of a university building at the height of about 51 m a.g.l, hereafter called UWS. Air pressure (p) is measured by a barometer (model PTB110, Vaisala Oyj, Helsinki, Finland). T_a and relative humidity (RH) are measured by a housed and ventilated temperature and relative humidity probe (model CS215A, Campbell Scientific Inc. (CSI), Logan, UT, USA). Global solar radiation (K_{down}) is measured by a ventilated pyranometer (model CM21, Kipp & Zonen (K&Z), Deft, The Netherlands). Precipitation (P) is measured using a tipping-bucket rain gauge (model SBS500, CSI). Wind speed is measured by a cup anemometer (model 00.14576.250 004, Lambrecht, Göttingen, Germany) and wind direction by a wind vane (model W200P, CSI). Measurement data is aggregated to hourly values (sum for precipitation, otherwise average).

In addition to the mentioned meteorological parameters, U-Net is trained by two supplementary temporal predictors, solar elevation and declination angles, to address seasonality (Reda and Andreas, 2004, 2007; Van Doninck, 2016).

2.2.3. Sampling of training and test data

Training data for neural networks must be representative as neural networks are able to interpolate but not extrapolate. Therefore, it is crucial for the generalisability of the neural network to find a suitable sample of training data.

To select appropriate training areas, a grid is placed over the study area with a cell size of 500 × 500 m. Next, the proportions of land cover classes are calculated for each grid cell. The grid cells are then divided into 5 clusters using the k-means cluster algorithm. The clusters roughly represent urban areas, forests, meadows, and areas with a high proportion of open water / bare soil. In the final step, 50 grid cells are drawn randomly from these clusters with a focus on urban areas. In addition to these 50 sampled areas, 12 additional areas were added by hand to cover areas where measurements are available and ensure that Freiburg’s inner city, where most people are exposed to heat stress, is well represented (Fig. 1). Table 2 gives an overview of the properties of the test areas. The test areas were selected to cover measurement points of the KLIMES measuring campaign in 2007 / 2008. Of the 6 test areas, two areas represent residential areas with dominantly pre-1945 building structures (Wiehre, Herdern), two with new post-1990 building structures (Rieselfeld, Vauban), one the City Centre with larger buildings and open squares (City Centre) and one area an open field with large low-rise buildings (Airport).

Meteorological training data is drawn from the years 2018 and 2019. Similar to spatial data, meteorological data are first clustered by k-means cluster algorithm, and then, unlike spatial data, 64 days are equally drawn from these clusters. To cover extremes, days with average minimum and maximum T_a and days with absolute minimum and maximum T_a are added. Sampled data has an hourly

Table 1
Overview of the *T*mrt measurement campaign sitesin 2007 / 2008 with coordinates, measurement durations, sky view factors (SVF), and urban site characteristics.

Site name	Coordinates (Lat / Lon) (WGS84)	Start (UTC)	End (UTC)	SVF	City district
Open field	48.0233° / 7.8344°	2007-04-16 06:00	2007-04-18 11:00	0.99	Airport
Intersection	47.9748° / 7.8296°	2007-07-14 07:20	2007-07-15 06:00	0.73	Vauban
Street canyon (1)	47.9978° / 7.7922°	2007-06-19 08:00	2007-06-20 10:00	0.66	Rieselfeld
Street canyon (2)	47.9922° / 7.8446°	2007-05-24 07:50	2007-05-24 22:15	0.44	City centre
		2008-02-08 09:00	2008-02-08 17:30		
Street canyon (3)	47.9863° / 7.8439°	2007-07-16 07:20	2007-07-16 16:20	0.42	Wiehre
Tree-lined street	48.0062° / 7.8576°	2007-08-01 07:30	2007-08-01 21:30	0.23	Herdern
		2007-01-13 09:15	2007-01-13 16:30		

Table 2
Properties of test areas with local climate zone (LCZ), mean sky view factor (SVF), building and tree cover fractions, zero-plane displacement height, and mean building height.

City district	LCZ	SVF (mean)	Building cover fraction	Tree cover fraction	Zero-plane displacement height (m)	Mean building height (m)
Airport	LCZ 8/LCZ D	0.94	0.14	0.35	9.9	10.3
City centre	LCZ 5	0.64	0.44	0.22	22.8	15.2
Herdern	LCZ 6	0.71	0.28	0.49	15.7	12.6
Vauban	LCZ 6/LCZ D	0.84	0.18	0.38	11.8	9.7
Rieselfeld	LCZ 6	0.75	0.27	0.28	13.2	11.5
Wiehre	LCZ 6	0.71	0.30	0.49	14.6	11.3

resolution. Test data (12 days) are chosen based on the available data from the measurement campaign.

2.3. Physical T_{mrt} modelling using SOLWEIG

SOLWEIG is a 2.5-dimensional microscale model for simulating radiant fluxes and T_{mrt} in complex urban areas. A detailed documentation can be found in Lindberg et al. (2008, 2016a); Lindberg and Grimmond (2011, 2019); and Wallenberg et al. (2020). Various studies have been conducted to intercompare SOLWEIG to other microscale models and to evaluate model performance against six-directional radiation (Höppe, 1992; VDI, 1994) or black globe temperature measurement methods (Lindberg et al., 2008; Lindberg and Grimmond, 2011; Chen et al., 2014; Szűcs et al., 2014; Jänicke et al., 2015; Aminipouri et al., 2019a; Gál and Kántor, 2020; Liu et al., 2020; Wallenberg et al., 2020). SOLWEIG follows the six-directional approach of Höppe (1992) for calculating T_{mrt} by estimating short- and longwave radiation fluxes of six directions (upward, downward, and the four cardinal directions) for the height of 1.1 m a.g.l (hereafter referred to as "at pedestrian level"). T_{mrt} is computed for a standing or walking person (rotationally symmetric) with angular factors (weighting coefficients) of 0.22 for radiation fluxes from cardinal points and 0.06 for radiation fluxes from above and below (Lindberg et al., 2008). Angular factors describe the share of the human surface in a given direction.

SOLWEIG uses spatial 2D and meteorological input data (see section 2.2.2 Training data). Model parameters emissivity, albedo, transmissivity of light through vegetation and trunk height are set to default (Table 3) (Konarska et al., 2013; Lindberg et al., 2008). SOLWEIG takes gradual surface temperature (T_s) drop / rise into account when pixel changes from sun- days are used exposed to shaded (and vice versa) to adjust outgoing longwave radiation (Lindberg et al., 2008). To address for this effect, SOLWEIG is run with spin up time of one day. SOLWEIG is used to calculate T_{mrt} for 62 areas on 80 days resulting in 101,688 T_{mrt} maps.

2.4. U-Net model design

All modelling is done with Python (Python Software Foundation, https://www.python.org/) and PyTorch (Paszke et al., 2019). First, a brief description of data preparation is given before the used model architecture and the training process are presented. For a detailed description of CNN and U-Net see appendix A.

2.4.1. Data preparation

It is common practice in deep learning to normalize data before training neural networks, which usually improves accuracy. Therefore, both spatial predictors and T_{mrt} maps are standardized to have zero mean and unit variance:

$$X_{norm} = \frac{X - \mu}{\sigma}$$

With X as the predictor to be normalized, μ mean of X, and σ standard deviation of X. Temporal data is not normalized. For testing, predicted T_{mrt} is denormalized.

2.4.2. U-Net architecture

The U-Net architecture in this study generally follows the encoder-decoder architecture introduced by Ronneberger et al. (2015).

Table 3
Used model parameter for SOLWEIG and its pre-processors (default values).

Model parameter	Value
Emissivity	0.95 (ground) 0.9 (walls)
Albedo	0.15 (ground) 0.2 (walls)
Transmissivity	3%
Trunk height	25% of tree height

More specifically, the encoder passes an image (spatial predictors in this task) through a set of convolution and pooling layers to obtain meaningful feature maps and reduce the spatial dimensionality. After encoding, the feature maps are passed to the decoder for successive up-convolution layers. In this work, the architecture follows the design of Dosovitskiy et al. (2015), where pooling layers are removed and the spatial dimensions are reduced through convolutions with larger strides (e.g., stride 2). This approach allows a more specific down-sampling by 'learning' the pooling operation, which makes, on the other hand, decoding easier. Fig. 2 shows the used architecture schematically.

In the encoding part, spatial input data (21, 256, 256) are processed by a first convolutional layer with stride 1 (no reduction of spatial dimension) and 32 filters. The first layer is followed by three convolutional layers with stride 2 (reduction of spatial dimensionality of factor 2 per layer), increasing number of filters (factor 2 per layer) and kernel size 3, resulting in an abstract representation of the spatial input data with a dimension of (256, 32, 32). After spatial data is encoded, temporal data is added to the abstract spatial representation. Therefore, temporal data is transformed by a fully connected layer to obtain the same dimension as the spatial representation. The decoding part consists of three up-sampling layers, again with stride 2 and kernel size 3, for doubling spatial dimension. After each up-sampling layer, feature maps with the same dimensions of encoder and decoder are concatenated (skip connections), followed by a convolutional layer with a kernel size of 1 to half the number of feature maps again. These skip connections ensure the flow of information from the encoder to the decoder and result in less blurry outputs. After up-sampling, the last layer outputs a single T_{mrt} map by a convolutional layer with a kernel size of 3.

Except for the last one, each convolutional layer is followed by a batch-normalization and non-linearity layer (ReLU activation function - Table 4). Adaptive moment estimation (Adam) is chosen as the optimization algorithm (Kingma and Ba, 2015). The learning rate is set to 0.001 and an exponential decay of the learning rate after each batch is applied with gamma = 0.9999. Mean absolute error (MAE) is used as loss function:

$$MAE = \frac{1}{n}\sum_{i=1}^{n} \mid \widehat{Y}_i - Y_i \mid$$

With $\widehat{Y}_i$ as predictions and Y_i as true value. In addition to MAE, root mean square deviance (RMSE) is calculated as supplementary score for performance evaluation. As this study focuses on outdoor thermal comfort, rooftops are excluded from evaluation (but included in training).

2.4.3. Training

The U-Net is trained for 10 epochs with a batch size of 32. Each epoch uses all spatial and temporal training data. Batches of training data are randomly shuffled in each epoch. Random cropping is used during training with crop size of 256 × 256. After each epoch, model performance is determined. Therefore, test input resolution is resized from 500 × 500 to 256 × 256 using bi-linear down-

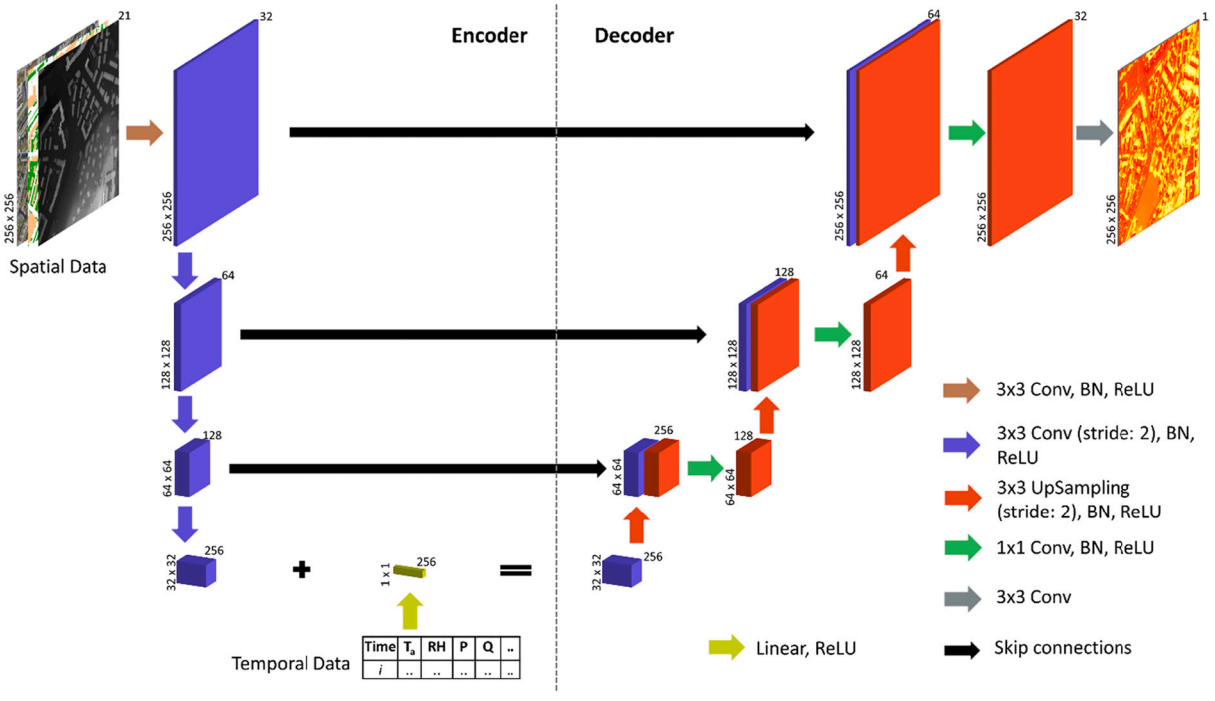

Fig. 2. Schematic visualization of the used U-Net approach: 2D Convolutional Layer (Conv), batch normalization (BN), ReLU activation function (ReLU), fractionally-strided convolution up sampling layer (UpSampling), linear transformation of temporal data (Linear). Temporal data is added to the compressed latent representation of the spatial input data.

Table 4
Used hyper-parameter of U-Net.

Hyper-parameter	Settings
Activation function	ReLU
Optimizer	Adam (learning rate: 0.001, gamma: 0.9999)
Loss function	L1 Loss (MAE)
Number of epochs	10
Batch size	32

sampling. However, for predicting and final model evaluation, the initial 500 × 500 raster data are split into four 256 × 256 subsets covering the entire 500 × 500 raster data. The four subsets are framed back together to a 500 × 500 extent for evaluation metrics calculation. Of the 62 areas, 6 are used as test areas, whereas 12 of the 80 days are used for testing. The remaining training data (56 areas and 68 days) are used for training the U-Net. This means training and test data consist of 91,392 and 10,296 T_{mrt} maps, respectively.

2.4.4. Computational performance evaluation

To evaluate the temporal performance of the U-Net, we compared the computing time from SOLWEIG and the U-Net for 720 timesteps (equal to 5 days with 10 min resolution, 30 days with hourly resolution) and a 500 × 500 m area. The computer used has the following specifications: Intel Core i9-9900KF CPU @ 3.60 GHz, 32 GB RAM, and a NVIDIA GeForce RTX 3080 (GPU). SOLWEIG uses the CPU while the U-Net is trained on the GPU.

2.5. Application: Long-term T_{mrt} modelling for Freiburg

As a potential application, ERA5-Land hourly reanalysis data (Muñoz Sabater, 2019, 2021) are used as temporal predictors to predict long-term T_{mrt} at pedestrian level. Windspeed and -direction, short-wave downwelling radiation, air pressure, T_a, and dewpoint temperature are extracted from ERA5-Land data for the centre point of the study area (47.9959° / 7.85222°, WGS84). Before the U-Net is driven with ERA5-Land data, the distributions and extreme values of ERA5-Land and measured data used for training were checked for agreement, because artificial neural networks can interpolate well but not extrapolate. Both data sets show good agreement except at extremely low T_a values. ERA5-Land includes data points below −10 °C (down to −24 °C), while the training data only includes data down to −10 °C. This means, predictions of cold extremes are not completely reliable. However, since the focus is on summertime T_{mrt} predictions anyway, this does not affect the results of the application. The study area has a size of 6 × 6.5 km with a resolution of 1 m and covers almost the entire urbanized area of Freiburg. The model is run at an hourly time step for two complete climate reference periods (1961–1990 and 1991–2020) for the months June, July, and August from 6:00 to 20:00, resulting in >10 million simulations.

Table 5
Evaluation metrics of measurement sites (U-Net, SOLWEIG, and measurements). RMSE is root mean square error, MAE is mean absolute error. (S) and (W) describe summer and winter measurements. (n) gives the number of observations used for the evaluation metric calculation for each site and combination.

Site	U-Net vs Measurements		SOLWEIG vs Measurements		U-Net vs SOLWEIG	
	RMSE (K)	MAE (K)	RMSE (K)	MAE (K)	RMSE (K)	MAE (K)
Open field (n = 246, 246, 429)	5.1	4.1	4.4	3.6	2.3	1.6
Intersection (n = 135, 135, 286)	6.2	4.7	7.1	4.6	6.1	3.6
Street canyon (1) (n = 157, 157, 286)	6.8	4.9	6.2	5.0	6.9	3.9
Street canyon (2) (S) (n = 102, 102, 143)	4.2	3.3	6.5	4.4	3.9	2.2
Street canyon (2) (W) (n = 53, 53, 143)	7.1	4.6	6.8	4.2	0.5	0.3
Street canyon (3) (n = 84, 84, 143)	4.7	3.7	5.3	4.1	4.5	2.2
Tree-lined street (S) (n = 85, 85, 143)	6.4	4.8	8.0	5.4	5.3	1.8
Tree-lined street (W) (n = 45, 45, 143)	4.8	4.5	4.6	4.1	0.6	0.4
Overall	5.7	4.3	6.0	4.4	4.6	2.3

3. Results

A direct validation of the model results on pointwise measurements is given in section 3.1. A detailed area-wise comparison between the physical model (SOLWEIG) and the U-Net is given in section 3.2. Results of the application of the U-Net for modelling climate changes at urban scale are shown in section 3.3.

3.1. Pointwise validation of SOLWEIG and U-Net based on measurements

A comparison of measurements and models for the six sites is given in Table 5. Fig. 3 shows the results for the sites "Open field" (Airport), "Street canyon (1)" (Rieselfeld), and "Intersection" (Vauban). At the site "Open field" (Fig. 3 (a)), measured and modelled T_{mrt} values at pedestrian level show a high concordance, apart from the first night where both models overestimate T_{mrt} by 5–10 K compared to the measurements. In the late morning and afternoon of 17 April (and 18 April), both models underestimate T_{mrt} by 3–4 K. MAE errors of U-Net / measurements and SOLWEIG / measurements are 4.1 K and 3.6 K, while MAE of U-Net / SOLWEIG is lower at 1.4 K. Fig. 3 (b) shows measurements and model predictions for the site "Street canyon (1)". Around 9:00 on the first day, both SOLWEIG and U-Net start to overestimate T_{mrt} at pedestrian level up to 9 K (SOLWEIG). While SOLWEIG overestimates T_{mrt} up to 5 K throughout the afternoon, U-Net results are in accordance with the measurements before U-Net underestimates T_{mrt} by almost 20 K (15:30–18:30. After sunset, T_{mrt} is underestimated by both U-Net and SOLWEIG by 5 K. MAE of U-Net / measurements and SOLWEIG / measurements are 4.9 K and 5.0 K, respectively. A comparison for a hot summer day at the site "Intersection" is shown in Fig. 3 (c). In the morning of the first day, U-Net and SOLWEIG start to overestimate T_{mrt}. At midday both models overestimate T_{mrt} (U-Net up to 12 K, SOLWEIG up to 20 K). In the afternoon, measured T_{mrt} values increase, so that U-Net underestimates T_{mrt}, while SOLWEIG continues to overestimate. Similar to Fig. 3 (b), U-Net estimates T_{mrt} lower than SOLWEIG in the afternoon. In the evening and night, measurements and modelled T_{mrt} are in accordance. MAE error of U-Net / measurements and SOLWEIG / measurements are 4.7 K and 4.6 K. The overall MAE for U-Net is 4.3 K and 4.4 K for SOLWEIG. Overall, MAE between U-Net and SOLWEIG is low at 2.3 K. In addition, both models estimate T_{mrt} less accurate when forced with ERA5-Land data.

Results of the remaining sites and detailed descriptions can be found in the supplementary material (S2 – Pointwise validation of SOLWEIG and U-Net based on measurements: remaining sites, Fig. S2-a, and Fig. S2-b).

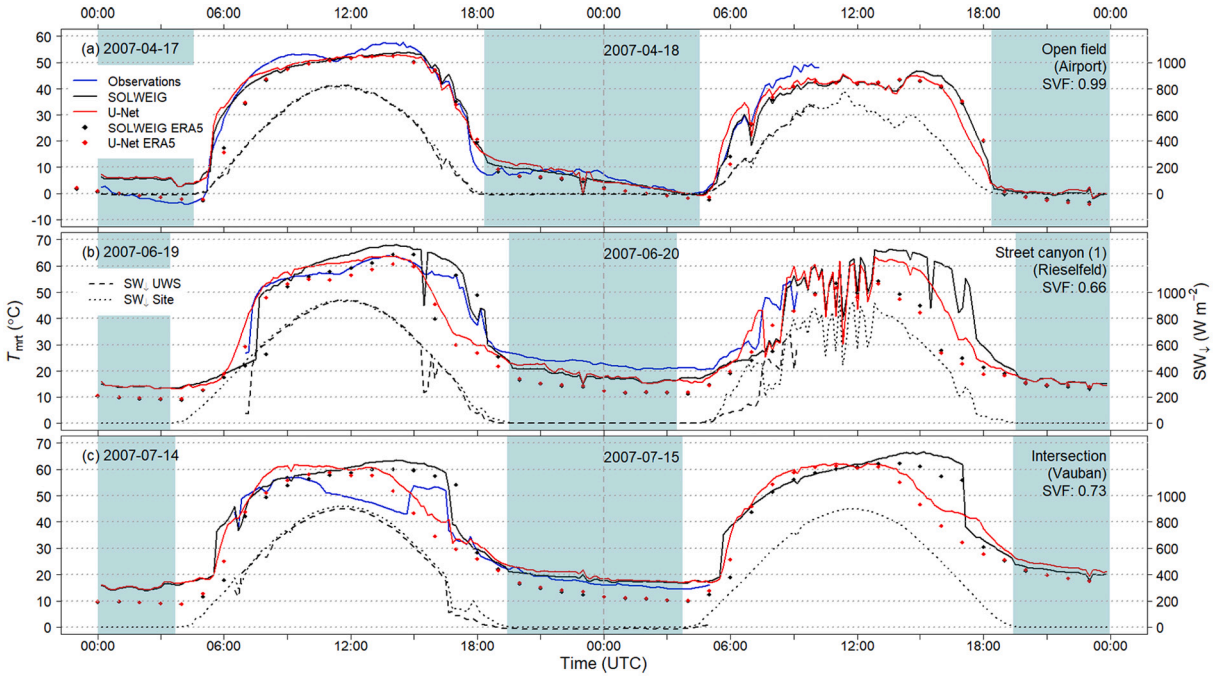

Fig. 3. T_{mrt} model predictions and stationary measurements for the sites "Open field", "Street canyon (1)", and "Intersection" for two diurnal cycle on April 16–18, 2007, June 19–20, 2007, and July 14–15, 2007, respectively forced with data from the urban weather station. Dashed black lines are downwelling shortwave radiation of the forcing data from the urban weather station ($SW_{\downarrow}$ UWS) and measured on site ($SW_{\downarrow}$ Site). Dots show model results with ERA5-Land forcing data. Blue shaded areas indicate nighttime hours. Observational data are not covering the entire two-day periods. SVF is sky view factor. (For interpretation of the references to color in this figure legend, the reader is referred to the web version of this article.)

3.2. Comparison of computational performance

The U-Net is about 22 times faster than SOLWEIG when saving predictions to GeoTIFF format. However, if the predictions are stored only in NumPy arrays, the U-Net is up to 38 times faster. For pure spatial statistics, calculated directly from the predictions, the U-Net is up to 130 times faster (e.g., Fig. 9). The U-Net needs 0.17 s for saving the output in NumPy format and 0.29 in GeoTIFF format, while SOLWEIG needs 6.50 s for calculating and saving a T_{mrt} map with a resolution of 500 × 500 m.

3.3. Area-wide validation of U-Net against SOLWEIG

A direct comparison of U-Net and SOLWEIG predictions is shown in two levelplots (Fig. 4 and Fig. 5) and Table 6. Fig. 6 shows predicted T_{mrt} maps at pedestrian level of both models and their differences for four time steps. T_{mrt} prediction error (MAE) of the U-Net as a function of time, season, area, solar elevation angle, and spatial resolution are shown in Fig. 7, Fig. 8, and Fig. 9.

Fig. 4 shows U-Net predictions in relation to SOLWEIG predictions, expressed in occurrence frequencies. The highest frequencies are in line with the identity line, showing the good overall performance of the U-Net. The overall MAE of all areas at 2.4 K validates the good performance. MAE ranges from 2.0 K for Vauban area with a low building area fraction and high grass / tree area fractions to 2.6 K for Rieselfeld area with higher building area fraction and lower SVF (Table 2 and Table 6). Fig. 4 indicates, however, a slight underestimation of the U-Net for high T_{mrt} values (60–70 °C). A linear model fitted on SOLWEIG and U-Net data supports this visual impression, as its slope of 0.94 is smaller than 1. Fig. 5 shows the differences of normalized SOLWEIG and U-Net predictions in relation to normalized SOLWEIG predictions. The difference tends to be positive for high T_{mrt} values, while it is generally negative for low T_{mrt} values indicating that the U-Net has a systematic bias when predicting extreme values.

A diurnal cycle of SOLWEIG (a – d), U-Net (e – h), and their difference (i – l) by four time steps (06:00, 12:00, 18:00, 24:00 UTC) is shown in Fig. 6. Both models take land cover classes into account, resulting in lower T_{mrt} predictions over grass and water or under trees compared to paved surfaces (e.g., compare b, f with m). Predictions for the night agree (d, h and l), while the predictions for the day show differences. SOLWEIG predictions have a sharper transition from shadow to light (a – c) than U-Net predictions, which can be seen by the more blurry-looking transitions of the U-Net (e – g). Fig. 6 (j) illustrates the problem of the U-Net in predicting the transitions from shadow to light, as high positive and low negative differences are close to each other. At times with low solar elevation angle (i and k), large prediction differences cover more pixels and thus greater areas, which can be seen in the East-West canyon (k), and the underestimation of T_{mrt} by the U-Net for already sunlight areas in (i).

The impact of area, season and time on U-Net T_{mrt} predictions are shown in Fig. 7. As indicated in Fig. 6 (i) and (k), time of day has a strong impact on model performance of the U-Net. Fig. 7 (a – c) show MAE aggregated for each area and season as a function of time. MAE values follow different diurnal cycles for each area and season. MAE is higher at noon in winter than in spring or summer. In spring, however, MAE is higher in the morning and evening than in summer. The diurnal MAE curves for spring and summer also show that areas with lower building cover fraction and higher SVF (Vauban and Airport) have lower MAE throughout the day than areas with higher building cover fraction and lower SVF (Wiehre, Herdern, Rieselfeld, and City Centre). In Winter, however, MAE of the Airport area is higher. It can be seen that diurnal MAE curves follow a seasonal pattern, with the highest MAE at noon in winter and the highest MAE in the morning and evening in spring and summer. Aggregated MAE by season (Fig. 7 (d)) shows this seasonal pattern of the diurnal MAE cycles more precisely.

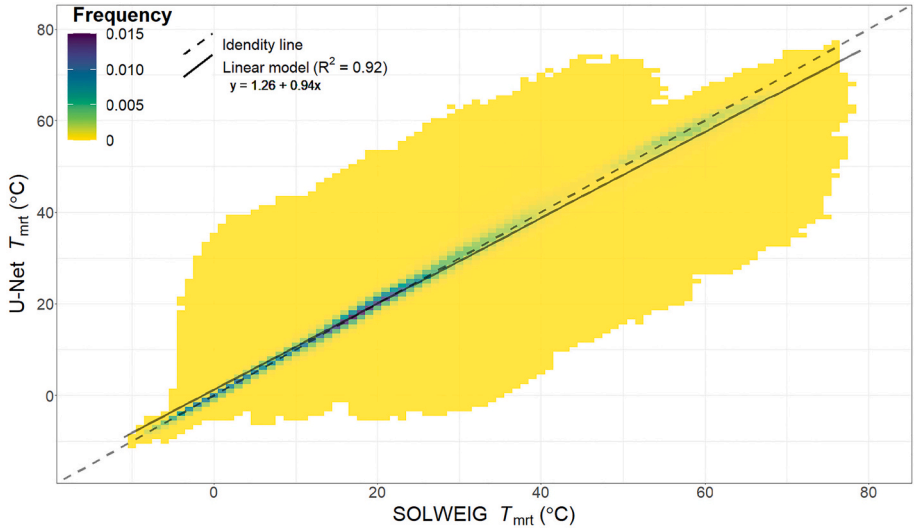

Fig. 4. Levelplot of U-Net predictions in relation to SOLWEIG predictions. Color indicates the frequency of occurrence; dashed line is the identity line (1:1 line) and solid line is a linear model fitted on U-Net predictions as a function of SOLWEIG predictions. The 95% confidence interval of the slope cannot be seen, because it's to narrow.

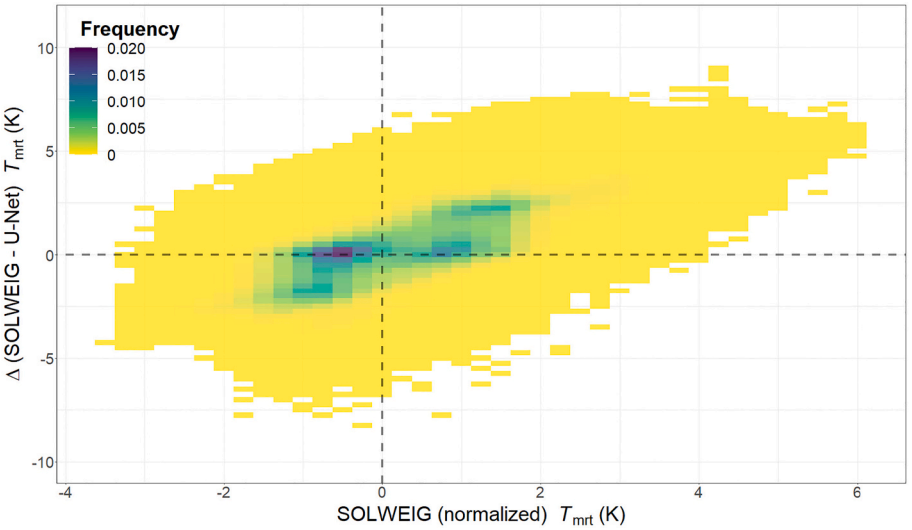

Fig. 5. Levelplot of the difference of normalized SOLWEIG and U-Net predictions in relation to normalized predictions by SOLWEIG. The color indicates the frequency.

Table 6
Evaluation metrics of the test areas (SOLWEIG vs. U-Net). RMSE is root mean square error and MAE is mean absolute error.

Area	RMSE (K)	MAE (K)
Airport	3.4	2.2
City centre	4.0	2.5
Herdern	3.9	2.3
Rieselfeld	4.1	2.6
Vauban	3.5	2.0
Wiehre	4.0	2.5
Overall	3.8	2.4

The variation in model performance depending on season and time is related to the solar elevation angle. Fig. 8 shows a clear connection between solar elevation angle and model performance (MAE). While MAE is low at low sun elevation angles, MAE values increase at moderate elevation angles (20–40°) before decreasing again at high sun elevation angles.

3.4. U-NNet application – Downscaling T_{mrt} for two climate reference periods

To demonstrate the potential of the U-Net model for climate change applications at the urban scale, we run 60 years of daytime T_{mrt} at hourly resolution in summer for the city of Freiburg (see Section 2.3 and Appendix B for results of the entire urbanized area of Freiburg). In this case, the individual output maps are not saved, but T_{mrt} statistics are summed up during the model run.

The results of long-term modelled T_{mrt} for a subset of Freiburg are shown in Fig. 9 and Fig. 10. Fig. 9 (a – c) compares the average summertime daily maximum T_{mrt} at pedestrian level (months June, July, and August) for two periods (1961–1990 and 1991–2020). Fig. 9 (d – e) shows average hours per year with $T_{mrt} \geq 60$ °C for the two reference periods. The threshold value of 60 °C is chosen because it corresponds to a physical equivalent temperature (PET) of ≥40 °C and thus to severe heat stress (Lee et al., 2013; Thorsson et al., 2017). Average summertime daily maximum T_{mrt} at pedestrian level increases within the entire area of Freiburg (Fig. 9 (c) and Fig. B1 (a)) by an average of 2.5 K (Table 7) while ranging from 1.1 K to 4.0 K from the first to the second period. Average summertime daily maximum T_a, however, increases by only 1.5 K in the same period (in the ERA5-Land data). Pixels covered by tree canopy (dark blue pixels in (a) and (b)) experience a smaller T_{mrt} increase than pixels without tree cover (1.7 K compared to 2.7 K). On a daily average, however, T_{mrt} increases by 1.7 K, which is less than the average daily maximum value of T_{mrt}, with the increase being somewhat smaller in shady areas than in sunlit areas (Table 7). The number of hours per year and pixel with $T_{mrt} \geq 60$ °C increase with an average of 6 h from period one to period two, with the highest increase (by up to 90 h / doubling its values) to the south of buildings (Fig. 9 d – f). Similar to the average daily maximum T_{mrt}, hours with $T_{mrt} \geq 60$ °C increase more in areas without trees and paved surfaces and less in parks with tree cover and grassy areas. Days with average $T_{mrt} \geq 60$ °C of the entire 500 × 500 area increase from

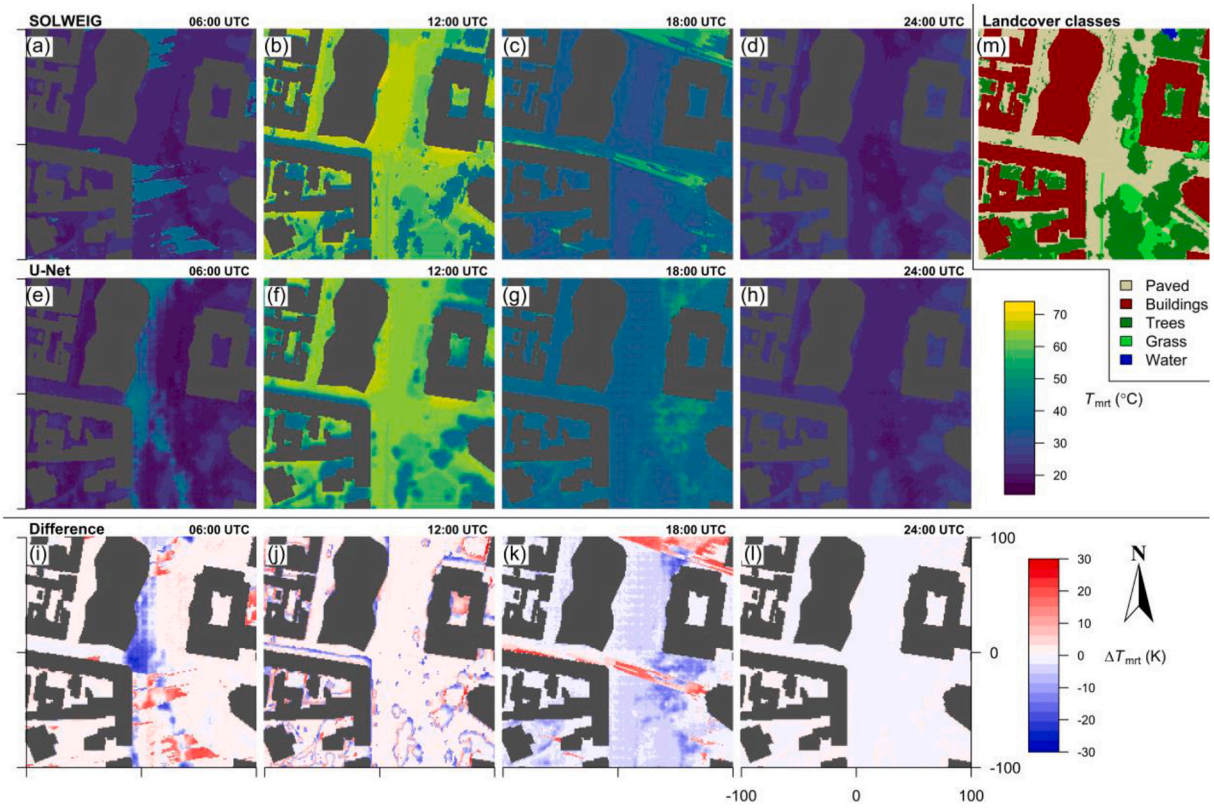

Fig. 6. This figure shows a 200 × 200 m subset of a modelled T_{mrt} map at a height of 1.1 m a.g.l. and a spatial resolution of 1 × 1 m by SOLWEIG (a – d) and U-Net (e – h), as well as the difference (i – l) for four time steps of a clear summer day (July 17, 2007) in the city centre of Freiburg. (m) shows land cover classes of the area. Coordinates of each figure center are 47.9938° / 7.84523° (WGS84).

1.3 to 4.3 from period one to period two. Fig. 10 shows the average number of hours per year in T_{mrt} classes within the 30-year periods. The classes comprise 5° bins (e.g., 5–10 °C, 10–15 °C, etc.). While the number of hours decreases in classes with T_{mrt} values below 10 °C, the number of hours increases in classes with T_{mrt} values above 10 °C, with the highest relative increase (up to 3 times) in classes between 50 and 70 °C.

4. Discussion

4.1. Pointwise validation of SOLWEIG and U-Net based on measurements

SOLWEIG has been thoroughly validated for various cities (see section 2.3). From these studies, it can be concluded that microscale urban characteristics and weather conditions (clouds, solar radiation) strongly influence T_{mrt}. As SOLWEIG has already been validated, the focus of this study is not on a detailed model evaluation of SOLWEIG, but on demonstrating that the performance of SOLWEIG (and U-Net) is consistent with the results of previous studies. The results of the station "open field" at the airport area show the good performance of SOLWEIG and U-Net on a clear sky day in a non-complex environment (Fig. 3 (a)). As the complexity of surroundings increases due to buildings and trees, both models become less accurate or cannot accurately represent every T_{mrt} variation (Fig. 3 (b) (c) and Fig. S2 and S3). Reasons for the reduced accuracy are the more complex shadowing and emissivity with increasing building / tree cover that are not fully represented in the input data. Nevertheless, the accuracy of SOLWEIG (and U-Net) is in line with literature, which ranges between 2.7 and 5.8 K for MAE (Lindberg and Grimmond, 2011; Jänicke et al., 2015; Kántor et al., 2018; Aminipouri et al., 2019a; Gál and Kántor, 2020) and 4.4–4.8 K (RMSE) (Lindberg et al., 2008, 2016a). A more detailed discussion can be found in supplementary material S2.

The difference between U-Net and SOLWEIG predictions is much smaller than between SOLWEIG and measurements. This means that improving the U-Net model would require, in the first step, a more precise model calibration of SOLWEIG (emissivity, albedo, and transmissivity) and/or more detailed spatial input data or improved physics in SOLWEIG.

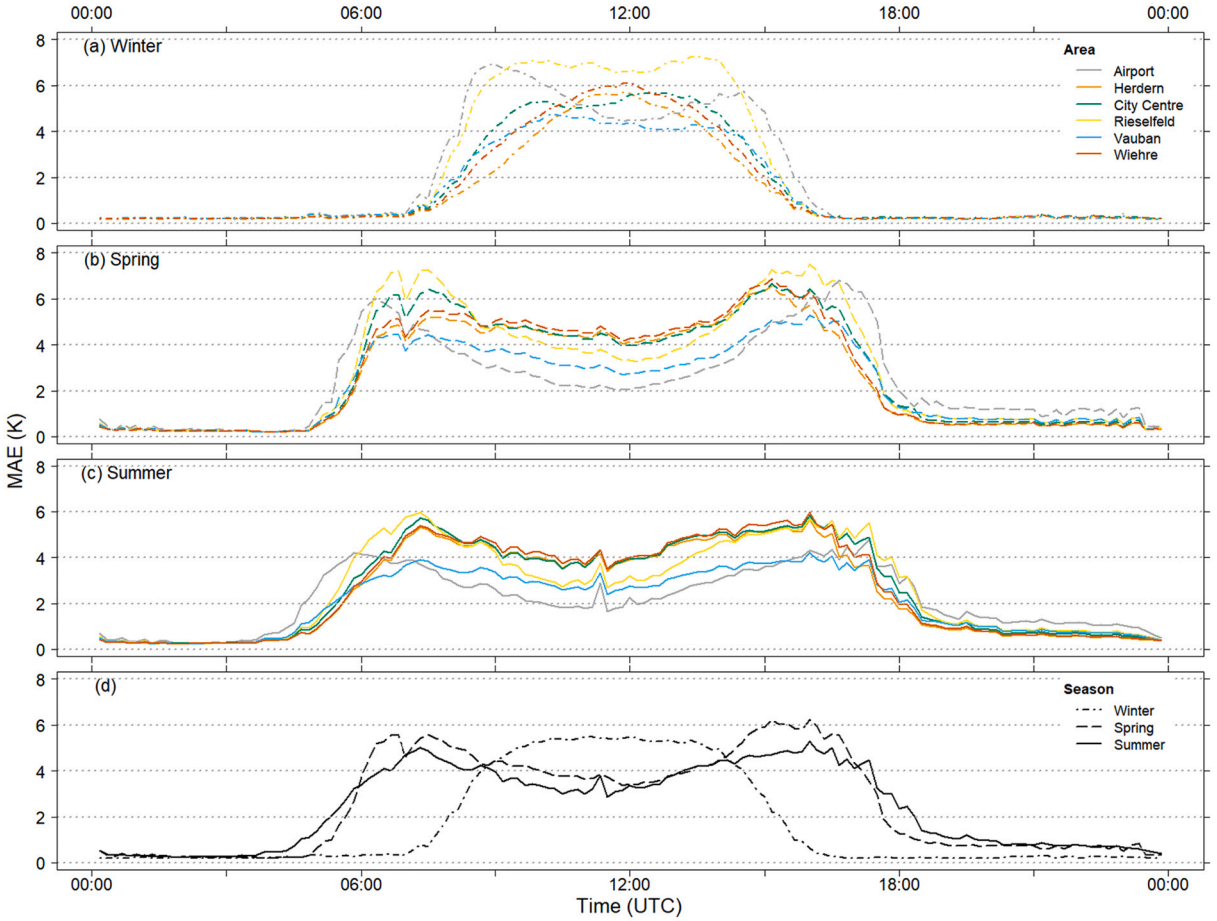

Fig. 7. MAE as a function of time aggregated by season and areas (a), days (b), and seasons (c). Spring covers the days April 16–18, 2007; Winter covers the days of 13. January 2008 and 8 February 2008; Summer covers the rest of the days. Color chart in (b) follows annual cycle (black: winter solstice; light-grey: summer solstice).

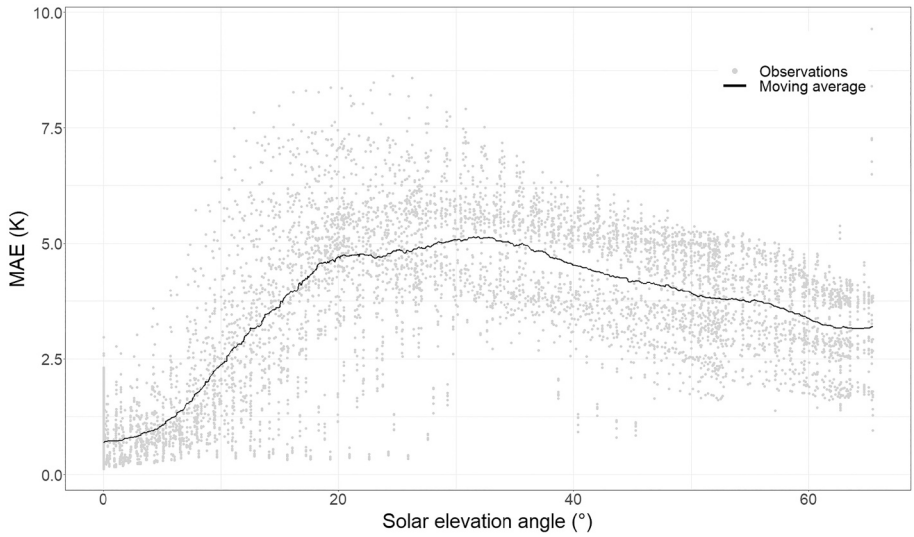

Fig. 8. MAE as a function of solar elevation angle. Each point represents a MAE value for one timestep and one area. The black line represents the moving average value of MAE (window size of 2.5°).

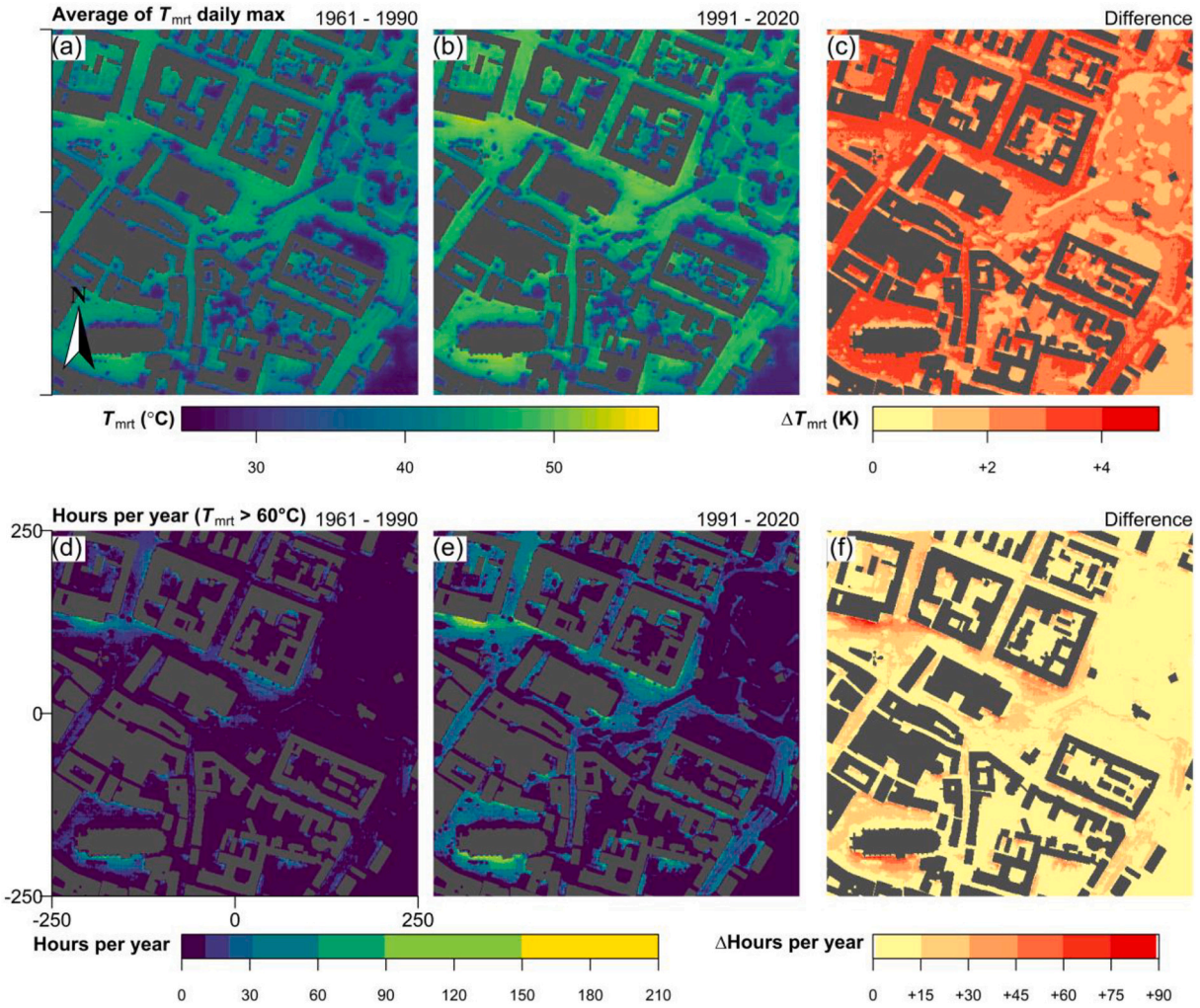

Fig. 9. Maps of average daily maximum T_{mrt} of the three summer months June, July, and August (JJA) for two climate reference periods (a, b) in a 500 × 500 m subset of central Freiburg. Second line shows hours per year with $T_{mrt} \geq 60$ °C (Thorsson et al., 2017) for the two periods (d, e). (c) and (f) show the corresponding differences between 1961–1990 and 1991–2020. Coordinates of each figure center are 47.9971° / 7.85495° (WGS84) with a 1 × 1 m resolution, north arrow is located in (A).

4.2. Area-wise validation of U-Net against SOLWEIG

Model performance of the U-Net is good, with an overall MAE of 2.4 K in relation to SOLWEIG (ranging from 2.0 to 2.6 K between test areas), highlighting the ability of deep neural networks to model T_{mrt} on unknown data and so in emulating complex physical models. Although MAE values are higher during the day than at night, MAE ranges are relatively low between 2 and 4 K during times with the highest risk of thermal stress (around midday in summer).

To the authors' knowledge, encoder-decoder networks such as U-Nets have not been used yet for modelling meteorological variables on micro-scales. However, U-Nets have been used on meso- and synoptic scales for different meteorological tasks. Sha et al. (2020) used a U-Net and a modified U-Net (U-Net-Autoencoder) to downscale maximum and minimum T_a from 0.25° (~ 28 km) to 4 km in Northern America. Sha et al. (2020) report that the used architecture leads to promising results in the downscaling of maximum and minimum T_a.

The U-Net performs better in open areas than in complex urban surroundings (Table 6, Fig. 7), because of the more complex shadowing in urban environments. SOLWEIG uses shadow matrices of the total sky vault (145 patches), while U-Net is trained only with aggregated shadow matrices (SVF factor maps) of the different cardinal points, making it much more difficult for the U-Net to model T_{mrt} as accurately as SOLWEIG. Wallenberg et al. (2020) point out the importance of the appropriate sky vault model for modelling T_{mrt} with SOLWEIG. The limitations of the U-Net modelling T_{mrt} at the transition from shadow to sun can also be seen in

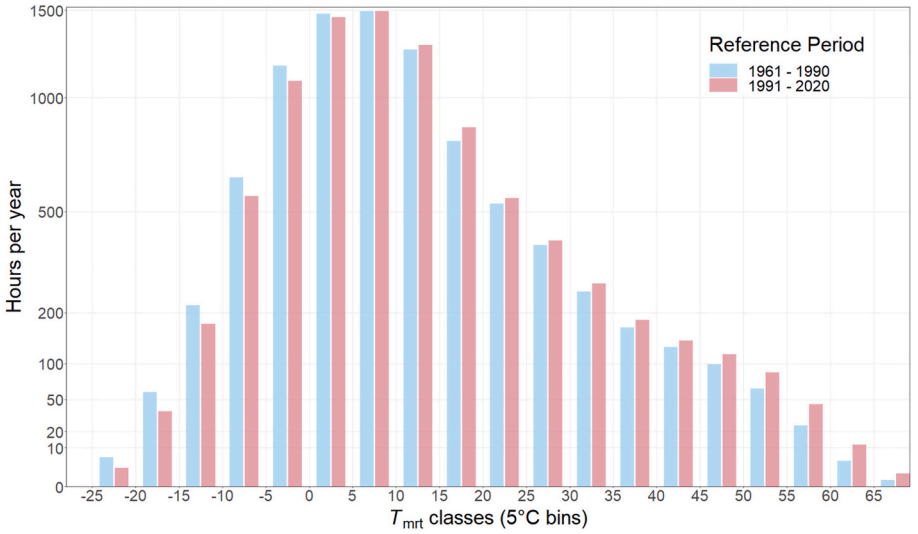

Fig. 10. Hours per year (averages for 500 × 500 m images) within T_{mrt} classes with a magnitude of 5 °C for two reference periods (1961–1990 and 1991–2020).

Table 7
Increase of average daily maximum T_{mrt} and average T_{mrt} for June, July, and August for different land cover classes for the entire urbanized area of Freiburg depicted in Fig. B1 from 1961–1990 to 1991–2020.

Land cover class	Average increase of daily maximum T_{mrt} (K)	Average T_{mrt} increase (K)
Covered by tree / grass	1.8	1.4
Covered by tree / paved	2.1	1.5
Covered by tree / all	1.9	1.5
Uncovered / grass	2.4	1.8
Uncovered / paved	2.8	1.9
Uncovered / all	2.7	1.8
All	2.5	1.7

Fig. 6 (i-k). Nevertheless, as the U-Net can reliably predict T_{mrt} without explicit shadow matrices, it can be assumed that providing the shadow matrices would significantly improve the performance of the U-Net. Kong et al. (2022) found a higher correlation of T_{mrt} on shadow patterns in the morning and evening, indicating the importance of exact shadow patterns. The highest prediction errors occur in the morning and evening on summer days and during midday on winter days (Fig. 6 and Fig. 7). The main reason for these diurnal error cycles is complex shadow patterns for low solar zenith angles. Low solar zenith angles create long shadowing of buildings and trees and thus affect a larger area. As the U-Net has its highest errors at the transition from shadow to sun, large errors and errors in a larger area occur under these circumstances. Fig. 8 shows the dependence of the model error as a function of solar zenith angle. The highest model errors occur for low solar zenith angles corresponding to morning / evening hours in summer and midday in winter. The U-Net underestimates high T_{mrt} and overestimates low T_{mrt} values (Fig. 4 and Fig. 5). Although training data were selected to cover the entire possible predictor space, extremes of sampled T_{mrt} data might not be represented enough in the training data.

The architecture and hyper-parameter of the U-Net have not been optimized yet, but have been selected to the best of the authors' knowledge. Additionally, the mentioned limitations of the U-Net are mostly related to the used spatial and temporal predictors: shadow matrices used by SOLWEIG were not used by the U-Net, and meteorological training data may not adequately represent all weather situations. Nevertheless, the U-Net shows a good performance which allows long-term analysis of T_{mrt} in urban areas. An improvement of the model could be achieved by optimising architecture and hyper-parameter, more detailed spatial predictors, and better sampled meteorological predictors.

4.3. U-Net application – Predicting T_{mrt} for two climate reference periods

SOLWEIG has already been used to compare long-term periods and how climate change affects T_{mrt} in urban areas (Lindberg et al., 2016b; Thorsson et al., 2017; Aminipouri et al., 2019b). However, as SOLWEIG is computationally intensive, previous studies have had to accept limitations in the calculations of T_{mrt}. Lindberg et al. (2016b), Thorsson et al. (2017), and Aminipouri et al. (2019b) used several decades of meteorological data with an hourly resolution for their analysis. In a first step, they calculated T_{mrt} for only one

generic point for the entire study period to analyse changes over time (SOLWEIG1D). In the second step, T_{mrt} was calculated for an entire area (SOLWEIG2D) for selected hours / days with $T_{mrt} \geq 60$ / 55 °C from step one. This means that spatial variability of T_{mrt} is always represented by predictions for single or multiple hours / days, but not for entire periods. The approach in this study overcomes these limitations using encoder-decoder networks such as the proposed U-Net. The computational superiority of the U-Net introduced in this study allows predictions for entire maps at the highest details for decades with manageable computational resources.

To demonstrate this application, U-Net was used to model T_{mrt} for a 6 × 6.5 km area in Freiburg for two periods (1961–1990 and 1991–2020) with ERA5-Land data (hourly resolution). Fig. 3 shows that both SOLWEIG and U-Net produce reasonable results when forced with ERA-Land data. Even if no future climate projections are presented here, the analysis of the changes between the references periods 1961–1990 and 1991–2020 gives an overview of what contributes to mitigating heat stress, especially as the results show the influence of land cover and shading on T_{mrt}. Days with area-wise averaged $T_{mrt} \geq 60$ °C tripled from period one to period two, while T_a increased by 1.5 K. Continued T_a increase could lead to further doubling / tripling of days with $T_{mrt} \geq 60$ °C. The average daily maximum value of T_{mrt} at pedestrian level increased by 2.5 K in summer, with an increase of 2.8 K and 1.8 K for paved and shaded grassy surfaces, respectively. The most substantial increase of daily maximum T_{mrt} at pedestrian level can be seen in sun-exposed areas located in the south-east to the south-west of buildings with paved surfaces and without trees providing shade. Trees and grass covered areas significantly reduce maximum T_{mrt} and thus heat load on humans. These results confirm findings from previous studies (Lindberg et al., 2016b; Thorsson et al., 2017). However, average daily T_{mrt} increase depends less on shading or land cover than maximum T_{mrt} increase, assuming that mitigation measures of heat stress affect only maximum T_{mrt}. This means the distribution of T_{mrt} will shift towards higher T_{mrt} values, regardless of any mitigation measures. Nevertheless, the right measures can counteract the right skewness of the T_{mrt} distribution (and thus the maximum T_{mrt} values) (compare Fig. 10). While T_{mrt} can be used as a proxy variable for outdoor daytime thermal comfort in summer, T_a, relative humidity and wind also contribute to human thermal comfort, so adaptation measures should also consider these variables.

4.4. Computational performance and usability

The U-Net is 22 times faster than SOLWEIG with a MAE of 2.4 K. As spatial and temporal data is the same, pre-processing differences can be neglected while comparing both approaches. SOLWEIG can be assessed by the QGIS plug-in UMEP, which provides a detailed documentation and tutorials, which makes SOLWEIG more suited for case studies and users with limited coding experience. Nevertheless, if SOLWEIG is used within the “UMEP for processing” QGIS processing framework or as stand-alone python scripts, coding skills are required as well. This means, the U-Net then might become more suited, especially when analysing larger areas or longer time periods, as computation time is less. It should be also noted, that the U-Net is a “first-step” of an outdoor thermal comfort AI-model covering the T_{mrt} part.

5. Conclusion

This study introduces a deep learning approach using a subtype of encoder-decoder network (U-Net) to model pedestrian level T_{mrt} in complex urban environments by emulating the physical model SOLWEIG. This means, SOLWEIG is used to generate T_{mrt} maps as response data of the U-Net. The U-Net is trained on 56 areas (500 × 500 m) and 68 days (hourly resolution) and tested on 6 areas and 12 days (10-min resolution). The following three objectives that were to be addressed in this study could be achieved: 1. U-Net is able to generalize and model T_{mrt} on unknown areas and weather situations accurately; 2. U-Net is computationally fast with a positive trade-off between predictive uncertainty and computational speed; and 3. U-Net allows for computationally efficient long-term modelling of spatially distributed T_{mrt} in urban areas.

The U-Net is able to generalize and model T_{mrt} on unknown areas and weather situations accurately. SOLWEIG (and U-Net) are point-wise validated against measurements in summer and winter in a first step. The MAE between measurements and SOLWEIG is higher than MAE between SOLWEIG and U-Net (4.4 K vs. 2.3 K). After point-wise validation of SOLWEIG on measurements, the U-Net is validated on the entire 6 test areas and 12 test days. Model accuracy (MAE) of U-Net is high at 2.4 K in relation to SOLWEIG. Model accuracy varies between different test areas and days, while shadow patterns and solar elevation angle have the highest impact on accuracy. U-Net model improvement can be achieved by adding training data and optimising the hyper-parameter and model architecture. Whereas an improvement of the overall model results also depends on the performance of SOLWEIG, which would require a more accurate SOLWEIG model, as the U-Net cannot be better than the data it is trained on. As the model is developed for the area of Freiburg, a transfer to other cities would require a new validation.

The U-Net is 22 times faster than SOLWEIG (if predictions are stored in GeoTIFF format), but up to 130 times faster for only calculating spatial statistics directly from the predictions (e.g., results in Fig. 9). With its MAE of 2.4 K, it has a positive trade-off between predictive uncertainty and computational speed, in our opinion. This means that the proposed U-Net approach is able to emulate a micrometeorological physical model with computational superiority. The computational superiority of the U-Net allows further investigations of T_{mrt} in complex urban areas for entire cities and decades.

The application of the U-Net on the urbanized area of Freiburg and two 30-year periods (1961–1990, 1991–2020) of ERA5-Land

reanalysis data with hourly resolution shows that summertime daily maximum T_{mrt} at pedestrian level increased by 2.5 K, whereas summertime daily maximum T_a increased by only 1.5 K from period one to period two. Maximum T_{mrt} increase is stronger on non-tree covered paved areas than on tree covered grassy areas (2.8 K and 1.8 K). Average T_{mrt} increase shows no difference between land cover classes, indicating that adaption measures are essential for extreme events.

CRediT authorship contribution statement

Ferdinand Briegel: Data curation, Conceptualization, Methodology, Software, Visualization, Writing – original draft. **Osama Makansi:** Software, Writing – review & editing. **Thomas Brox:** Supervision, Funding acquisition, Writing – review & editing. **Andreas Matzarakis:** Writing – review & editing. **Andreas Christen:** Project administration, Funding acquisition, Supervision, Writing – review & editing.

Declaration of Competing Interest

The authors declare that they have no known competing financial interests or personal relationships that could have appeared to influence the work reported in this paper.

Data availability

The authors do not have permission to share data.

Acknowledgments

This research was funded by the German Federal Ministry for the Environment, Nature Conservation and Nuclear Safety (BMU) on the basis of a resolution of the German Bundestag as part of the 'KI-Leuchtturm' project 'Intelligence for Cities' (I4C). Validation data (T_{mrt}) used in this research was collected as part of the KLIMES ALUF project (FZK: 01LS05020) within the scope of the research initiative "klimazwei", funded by the German Federal Ministry of Education and Research (BMBF). The authors wish to thank Jutta Holst for providing the data.

Appendix A. About convolutional neural networks, encoder-decoder, and U-Nets

Convolutional Neural Networks (CNN) have been developed for image classification. In terms of computer vision, convolution is a matrix (kernel) operation on a patch of pixels (e.g. 3×3). A Gaussian filter, for example, uses a Gaussian function as convolution kernel. In a CNN, however, the kernel values (weights) are not fixed but learned to minimize a loss function (prediction error). In other words, the CNN 'learns' the weights during the training process and the weights store the CNN's 'knowledge'. Non-linearity is added after each convolutional layer by the activation function.

CNNs are usually built of several convolutional layers followed by non-linear activations and pooling layers for dimension reduction. A pooling layer reduces the size of the image by extracting either the maximum or average value from a matrix sliding over the image. By using a 2×2 matrix for pooling, the image size is reduced to a half. Due to convolution, non-linearity and pooling, CNNs are able to learn patterns regardless of their position in the image (translation invariant) (Szeliski, 2011). This makes CNNs more efficient and requires less training data than densely-connected networks as the same kernel is applied / slid over the input (Chollet and Allaire, 2018).

Fully convolutional encoder-decoder networks enable image-to-image processing and are often used for image segmentation, optical flow and depth estimation. The encoding sub-model consists of convolutional, activation, and pooling layers and extracts patterns on different spatial levels. This means, the encoder compresses the input image into a latent representation with a reduced spatial dimension (Chollet and Allaire, 2018). The decoder sub-model then decodes the compressed latent representation back to an image with its initial dimension. To this end, the decoder uses convolutional layers as well as upscaling convolutional layers, which can be simple copying of a value into an N x N block of pixels, linear interpolation or learned deconvolution. The encoder and decoder parts define a symmetrical structure and can solve either supervised or unsupervised tasks. However, encoder-decoder networks have one main limitation, where information are lost due to down-sampling and up-sampling, thus resulting in blurry outputs.

U-Nets overcome this by adding skip connections from the encoder to the decoder. This means, spatially rich information from the encoder is passed to the decoder by concatenating the up-sampled feature maps (of the decoder) with the corresponding ones from the encoder at the same level. Although U-Net was initially developed for semantic segmentations where a classification per-pixel is learned, it has been applied widely in other tasks where continuous per-pixel values need to be predicted, such as optical flow and depth estimation, hence the similarity to the task of this study.

Appendix B. Changes in T_{mrt} from 1961–1990 and 1991–2020 for the entire urbanized area of Freiburg

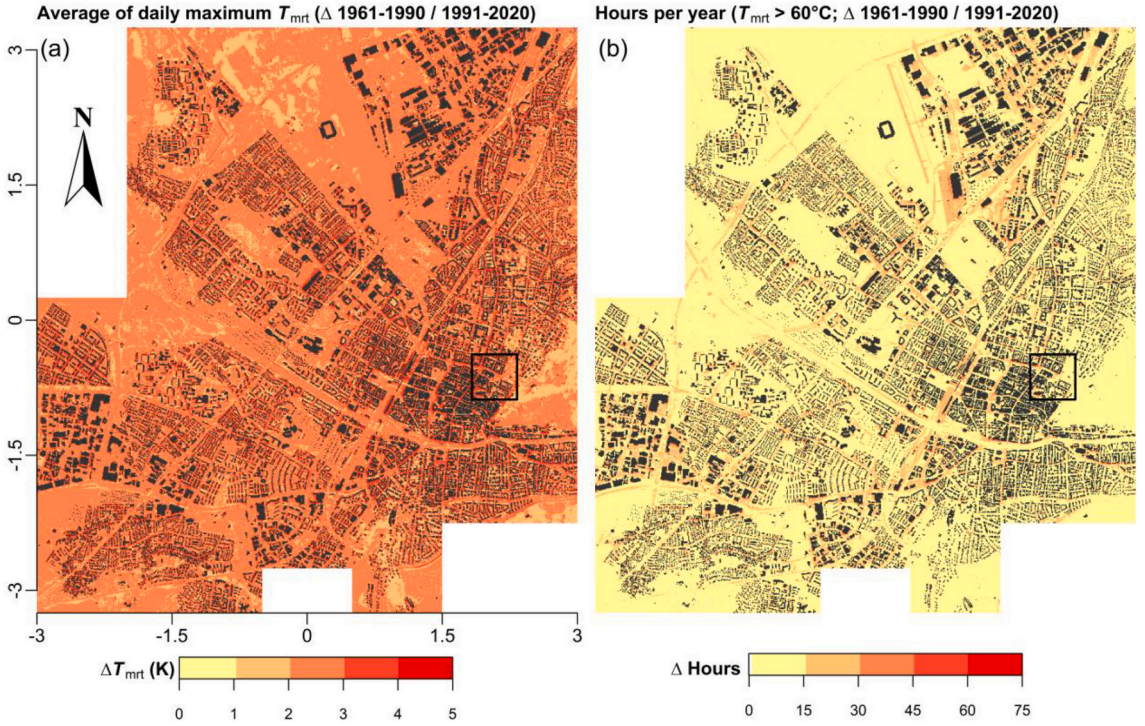

Fig. B1. Map of the difference of average daily maximum T_{mrt} of the three summer months June, July, and August (JJA) between 1961–1990 and 1991–2020 (a) and the difference of hours per year with $T_{mrt} \geq 60$ °C (b) of the urbanized area of Freiburg (6 × 6.5 km). Coordinates of each figure center are 48.0026° / 7.82694° (WGS84) with a 1 × 1 m resolution. More detailed results for the black square are shown in Fig. 9.

Appendix C. Supplementary data

Supplementary data to this article can be found online at https://doi.org/10.1016/j.uclim.2022.101359.

References

Aminipouri, M., Knudby, A.J., Krayenhoff, E.S., Zickfeld, K., Middel, A., 2019a. Modelling the impact of increased street tree cover on mean radiant temperature across Vancouver's local climate zones. Urban For. Urban Green. 39, 9–17. https://doi.org/10.1016/j.ufug.2019.01.016.

Aminipouri, M., Rayner, D., Lindberg, F., Thorsson, S., Knudby, A.J., Zickfeld, K., Middel, A., Krayenhoff, E.S., 2019b. Urban tree planting to maintain outdoor thermal comfort under climate change: the case of Vancouver's local climate zones. Build. Environ. 158, 226–236. https://doi.org/10.1016/j.buildenv.2019.05.022.

Bindoff, N.L., Stott, P.A., AchutaRao, K.M., Allen, M.R., Gillett, N., Gutzler, D., Hansingo, K., Hegerl, G., Hu, Y., Jain, S., Mokhov, I.I., Overland, J., Perlwitz, J., Sebbari, R., Zhang, X., 2013. Detection and attribution of climate change: From global to regional. In: Stocker, T.F., Qin, D., Plattner, G.-K., Tignor, M., Allen, S.K., Boschung, J., Nauels, A., Xia, Y., Bex, V., Midgley, P.M. (Eds.), Climate Change 2013: The Physical Science Basis. Contribution of Working Group I to the Fifth Assessment Report of the Intergovernmental Panel on Climate Change. Cambridge University Press, Cambridge, United Kingdom and New York, NY, USA, pp. 867–952. https://doi.org/10.1017/CBO9781107415324.022.

Bruse, M., 1999. Die Auswirkungen kleinskaliger Umweltgestaltung auf das Mikroklima-Entwicklung des prognostischen numerischen Modells ENVI-met zur Simulation der Wind-, Tempertaur-, und Feuchteverteilung in städtischen Struckturen. PhD Thesis.. Ruhr-Universität Bochum, Universitätsbibliothek.

Chan, S.Y., Chau, C.K., 2019. Development of artificial neural network models for predicting thermal comfort evaluation in urban parks in summer and winter. Build. Environ. 164, 106364 https://doi.org/10.1016/j.buildenv.2019.106364.

Chen, Y.-C., Lin, T.-P., Matzarakis, A., 2014. Comparison of mean radiant temperature from field experiment and modelling: a case study in Freiburg, Germany. Theor. Appl. Climatol. 118, 535–551. https://doi.org/10.1007/s00704-013-1081-z.

Chollet, F., Allaire, J.J., 2018. Deep Learning with R, 1st ed. Manning Publications Co., Greenwich, CT, USA.

Cohen, P., Potchter, O., Matzarakis, A., 2012. Daily and seasonal climatic conditions of green urban open spaces in the Mediterranean climate and their impact on human comfort. Build. Environ. 51, 285–295. https://doi.org/10.1016/j.buildenv.2011.11.020.

Diz-Mellado, E., Rubino, S., Fernández-García, S., Gómez-Mármol, M., Rivera-Gómez, C., Galán-Marín, C., 2021. Applied machine learning algorithms for courtyards thermal patterns accurate prediction. Mathematics 9, 1142. https://doi.org/10.3390/math9101142.

Dosovitskiy, A., Fischer, P., Ilg, E., Häusser, P., Hazırbas, C., Golkov, V., V., D., Smagt, P., Cremers, D., Brox, T., 2015. FlowNet: Learning Optical Flow with Convolutional Networks. In: IEEE International Conference on Computer Vision (ICCV), pp. 2758–2766. https://doi.org/10.1109/ICCV.2015.316.

EEA, 2017. European Environment Agency, climate change, impacts and vulnerability in Europe 2016 - an indicator-based report. Copenhagen. https://doi.org/10.2800/534806.

EEA, 2018. European Environment Agency, © European Union. Copernicus Land Monitoring Service, Urban Atlas. https://land.copernicus.eu/local/urban-atlas.

Epstein, Y., Moran, D.S., 2006. Thermal comfort and the heat stress indices. Ind. Health 44, 388–398. https://doi.org/10.2486/indhealth.44.388.
Freiburg, 2018. City of Freiburg Im Breisgau - 3D-City-model Freiburg i. Br. - LoD1. https://metadaten.geoportal-bw.de/geonetwork/srv/api/records/164ceef4-6c67-4763-8100-c5799a2ea6d8.
Freiburg, 2019. City of Freiburg im Breisgau - Orthophoto. https://metadaten.geoportal-bw.de/geonetwork/srv/api/records/0ffe37f7-9656-4766-8e7d-eb9500b3084d.
Freiburg, 2021. City of Freiburg Im Breisgau - LIDAR data, Vermessungsamt.
Fröhlich, D., Matzarakis, A., 2018. Spatial estimation of thermal indices in urban areas—basics of the SkyHelios model. Atmosphere 9. https://doi.org/10.3390/atmos9060209.
Gál, C.V., Kántor, N., 2020. Modeling mean radiant temperature in outdoor spaces, a comparative numerical simulation and validation study. Urban Clim. 32, 100571 https://doi.org/10.1016/j.uclim.2019.100571.
Holst, J., Mayer, H., 2011. Impacts of street design parameters on human-biometeorological variables. Meteorol. Z. 20, 541–552. https://doi.org/10.1127/0941-2948/2011/0254.
Höppe, P., 1992. Ein neues Verfahren zur Bestimmung der mittleren Strahlungstemperatur im Freien [a new procedure to determine the mean radiant temperature outdoors]. Wetter und Leben 44 (1–3), 147–151.
Jänicke, B., Meier, F., Hoelscher, M.-T., Scherer, D., 2015. Evaluating the effects of Façade greening on human bioclimate in a complex urban environment. Adv. Meteorol. 2015, 747259 https://doi.org/10.1155/2015/747259.
Jeong, S., Park, I., Kim, H.S., Song, C.H., Kim, H.K., 2021. Temperature prediction based on bidirectional long short-term memory and convolutional neural network combining observed and numerical forecast data. Sensors. https://doi.org/10.3390/s21030941.
Kántor, N., Unger, J., 2011. The most problematic variable in the course of human-biometeorological comfort assessment — the mean radiant temperature. Open Geosci. 3, 90–100. https://doi.org/10.2478/s13533-011-0010-x.
Kántor, N., Gál, C.V., Gulyás, Á., Unger, J., 2018. The impact of Façade orientation and Woody vegetation on summertime heat stress patterns in a central European Square: comparison of radiation measurements and simulations. Adv. Meteorol. 2018, 2650642. https://doi.org/10.1155/2018/2650642.
Kariminia, S., Shamshirband, S., Motamedi, S., Hashim, R., Roy, C., 2016. A systematic extreme learning machine approach to analyze visitors' thermal comfort at a public urban space. Renew. Sust. Energ. Rev. 58, 751–760. https://doi.org/10.1016/j.rser.2015.12.321.
Ketterer, C., Matzarakis, A., 2016. Mapping the physiologically equivalent temperature in urban areas using artificial neural network. Landsc. Urban Plan. 150, 1–9. https://doi.org/10.1016/j.landurbplan.2016.02.010.
Kingma, D.P., Ba, J.L., 2015. Adam: A Method for Stochastic Optimization. CoRR abs/1412.6.
Konarska, J., Lindberg, F., Larsson, A., Thorsson, S., Holmer, B., 2013. Transmissivity of solar radiation through crowns of single urban trees—application for outdoor thermal comfort modelling. Theor. Appl. Climatol. 117, 363–376. https://doi.org/10.1007/s00704-013-1000-3.
Kong, F., Chen, J., Middel, A., Yin, H., Li, M., Sun, T., Zhang, N., Huang, J., Liu, H., Zhou, K., Ma, J., 2022. Impact of 3-D urban landscape patterns on the outdoor thermal environment: a modelling study with SOLWEIG. Comput. Environ. Urban. Syst. 94, 101773 https://doi.org/10.1016/j.compenvurbsys.2022.101773.
Kreuzer, D., Munz, M., Schlüter, S., 2020. Short-term temperature forecasts using a convolutional neural network — an application to different weather stations in Germany. Machine Learning Appl. 2, 100007 https://doi.org/10.1016/j.mlwa.2020.100007.
Larraondo, P.R., Renzullo, L.J., Inza, I., Lozano, J.A., 2019. A data-driven approach to precipitation parameterizations using convolutional encoder-decoder neural networks. In: arXiv: Atmospheric and Oceanic Physics. https://doi.org/10.48550/arXiv.1903.10274.
Lee, H., Holst, J., Mayer, H., 2013. Modification of human-biometeorologically significant radiant flux densities by shading as local method to mitigate heat stress in summer within urban street canyons. Adv. Meteorol. 2013, 312572 https://doi.org/10.1155/2013/312572.
Li, D., Bou-Zeid, E., 2013. Synergistic interactions between urban Heat Islands and heat waves: the impact in cities is larger than the sum of its parts. J. Appl. Meteorol. Climatol. 52, 2051–2064. https://doi.org/10.1175/JAMC-D-13-02.1.
Lindberg, F., Grimmond, C.S.B., 2011. The influence of vegetation and building morphology on shadow patterns and mean radiant temperatures in urban areas: model development and evaluation. Theor. Appl. Climatol. 105, 311–323. https://doi.org/10.1007/s00704-010-0382-8.
Lindberg, F., Grimmond, C.S.B., 2019. SOLWEIG_v2019a. University of Gothenburg, Sweden, University of Reading, UK, Department of Earth Sciences.
Lindberg, F., Holmer, B., Thorsson, S., 2008. SOLWEIG 1.0 – Modelling spatial variations of 3D radiant fluxes and mean radiant temperature in complex urban settings. Int. J. Biometeorol. 52, 697–713. https://doi.org/10.1007/s00484-008-0162-7.
Lindberg, F., Onomura, S., Grimmond, C.S.B., 2016a. Influence of ground surface characteristics on the mean radiant temperature in urban areas. Int. J. Biometeorol. 60, 1439–1452. https://doi.org/10.1007/s00484-016-1135-x.
Lindberg, F., Thorsson, S., Rayner, D., Lau, K., 2016b. The impact of urban planning strategies on heat stress in a climate-change perspective. Sustain. Cities Soc. 25, 1–12. https://doi.org/10.1016/j.scs.2016.04.004.
Lindberg, F., Grimmond, C.S.B., Gabey, A., Huang, B., Kent, C.W., Sun, T., Theeuwes, N.E., Järvi, L., Ward, H.C., Capel-Timms, I., Chang, Y., Jonsson, P., Krave, N., Liu, D., Meyer, D., Olofson, K.F.G., Tan, J., Wästberg, D., Xue, L., Zhang, Z., 2018. Urban multi-scale environmental predictor (UMEP): an integrated tool for city-based climate services. Environ. Model. Softw. 99, 70–87. https://doi.org/10.1016/j.envsoft.2017.09.020.
Liu, D., Hu, S., Liu, J., 2020. Contrasting the performance capabilities of urban radiation field between three microclimate simulation tools. Build. Environ. 175, 106789 https://doi.org/10.1016/j.buildenv.2020.106789.
Matzarakis, A., Rutz, F., Mayer, H., 2007. Modelling radiation fluxes in simple and complex environments—application of the RayMan model. Int. J. Biometeorol. 51, 323–334. https://doi.org/10.1007/s00484-006-0061-8.
Matzarakis, A., Rutz, F., Mayer, H., 2010. Modelling radiation fluxes in simple and complex environments: basics of the RayMan model. Int. J. Biometeorol. 54, 131–139. https://doi.org/10.1007/s00484-009-0261-0.
Matzarakis, A., Martinelli, L., Ketterer, C., 2016. Relevance of thermal indices for the assessment of the urban Heat Island. In: Musco, F. (Ed.), Counteracting Urban Heat Island Effects in a Global Climate Change Scenario. Springer International Publishing, Cham, pp. 93–107. https://doi.org/10.1007/978-3-319-10425-6_4.
Mayer, H., 2008. KLIMES-a Joint Research Project on Human Thermal Comfort in Cities.
Mayer, H., Holst, J., Dostal, P., Imbery, F., Schindler, D., 2008. Human thermal comfort in summer within an urban street canyon in Central Europe. Meteorol. Z. 17, 241–250. https://doi.org/10.1127/0941-2948/2008/0285.
Middel, A., Nazarian, N., Demuzere, M., Bechtel, B., 2022. Urban climate informatics: an emerging research field. Front Environ Sci 10. https://doi.org/10.3389/fenvs.2022.867434.
Muñoz Sabater, J., 2019. ERA5-Land hourly data from 1981 to present. Copernicus Climate Change Service (C3S) Climate Data Store (CDS). (Accessed on <20.04.2022>). https://doi.org/10.24381/cds.e2161bac.
Muñoz Sabater, J., 2021. ERA5-Land hourly data from 1950 to 1980. Copernicus Climate Change Service (C3S) Climate Data Store (CDS). (Accessed on <20-04-2022>). https://doi.org/10.24381/cds.e2161bac.
Oh, J.W., Ngarambe, J., Duhirwe, P.N., Yun, G.Y., Santamouris, M., 2020. Using deep-learning to forecast the magnitude and characteristics of urban heat island in Seoul Korea. Sci. Rep. 10, 3559. https://doi.org/10.1038/s41598-020-60632-z.
Oke, T.R., Mills, G., Christen, A., Voogt, J.A., 2017. Urban Climates. Cambridge University Press. https://doi.org/10.1017/9781139016476.
OSM, 2017. OpenStreetMap contributors, Planet dump. retrieved from. https://planet.osm.org.
Paszke, A., Gross, S., Massa, F., Lerer, A., Bradbury, J., Chanan, G., Killeen, T., Lin, Z., Gimelshein, N., Antiga, L., Desmaison, A., Kopf, A., Yang, E., DeVito, Z., Raison, M., Tejani, A., Chilamkurthy, S., Steiner, B., Fang, L., Bai, J., Chintala, S., 2019. PyTorch: An imperative style, high-performance deep learning library. In: Wallach, H., Larochelle, H., Beygelzimer, A., Alché-Buc, F., Fox, E., Garnett, R. (Eds.), Advances in Neural Information Processing Systems 32. Curran Associates, Inc., pp. 8024–8035. https://doi.org/10.48550/arXiv.1912.01703
Potchter, O., Cohen, P., Lin, T.-P., Matzarakis, A., 2018. Outdoor human thermal perception in various climates: a comprehensive review of approaches, methods and quantification. Sci. Total Environ. 631–632, 390–406. https://doi.org/10.1016/j.scitotenv.2018.02.276.
Reda, I., Andreas, A., 2004. Solar position algorithm for solar radiation applications. Sol. Energy 76, 577–589. https://doi.org/10.1016/j.solener.2003.12.003.

Reda, I., Andreas, A., 2007. Corrigendum to “solar position algorithm for solar radiation applications” [solar energy 76 (2004) 577–589]. Sol. Energy 81, 838. https://doi.org/10.1016/j.solener.2007.01.003.

Ronneberger, O., Fischer, P., Brox, T., 2015. In: Navab, N., Hornegger, J., Wells, W.M., Frangi, A.F. (Eds.), U-Net: Convolutional Networks for Biomedical Image Segmentation BT - Medical Image Computing and Computer-Assisted Intervention – MICCAI 2015. Springer International Publishing, Cham, pp. 234–241. https://doi.org/10.48550/arXiv.1505.04597.

Seneviratne, S.I., Zhang, X., Adnan, M., Badi, W., Dereczynski, C., Luca, A. Di, Ghosh, S., Iskandar, I., Kossin, J., Lewis, S., Otto, F., Pinto, I., Satoh, M., Vicente-Serrano, S.M., Wehner, M., Zhou, B., 2021. Weather and Climate Extreme Events in a Changing Climate. In: Masson-Delmotte, V., Zhai, P., Pirani, A., Connors, S. L., Péan, C., Berger, S., Caud, N., Chen, Y., Goldfarb, L., Gomis, M.I., Huang, M., Leitzell, K., Lonnoy, E., Matthews, J.B.R., Maycock, T.K., Waterfield, T., Yelekçi, O., Yu, R., Zhou, B. (Eds.), Climate Change 2021: The Physical Science Basis. Contribution of Working Group I to the Sixth Assessment Report of the Intergovernmental Panel on Climate Change. Cambridge University Press, Cambridge, United Kingdom and New York, NY, USA, pp. 1513–1766. https://doi.org/10.1017/9781009157896.013.

Sha, Y., Gagne II, D.J., West, G., Stull, R., 2020. Deep-learning-based gridded downscaling of surface meteorological variables in complex terrain. Part I: daily maximum and minimum 2-m temperature. J. Appl. Meteorol. Climatol. 59, 2057–2073. https://doi.org/10.1175/JAMC-D-20-0057.1.

Staiger, H., Laschewski, G., Matzarakis, A., 2019. Selection of appropriate thermal indices for applications in human biometeorological studies. Atmosphere. https://doi.org/10.3390/atmos10010018.

Szeliski, R., 2011. Computer Vision: Algorithms and Applications, 1st ed. Springer, London. https://doi.org/10.1007/978-1-84882-935-0.

Szűcs, Á., Gál, T., Andrade, H., 2014. Comparison of measured and simulated mean radiant temperature. Case study in Lisbon (Portugal). Finisterra - Revista Portuguesa de Geografia 49, 95–111. https://doi.org/10.18055/Finis6469.

Thorsson, S., Rayner, D., Lindberg, F., Monteiro, A., Katzschner, L., Lau, K.K.-L., Campe, S., Katzschner, A., Konarska, J., Onomura, S., Velho, S., Holmer, B., 2017. Present and projected future mean radiant temperature for three European cities. Int. J. Biometeorol. 61, 1531–1543. https://doi.org/10.1007/s00484-017-1332-2.

Trebing, K., Stańczyk, T., Mehrkanoon, S., 2021. SmaAt-UNet: precipitation nowcasting using a small attention-UNet architecture. Pattern Recogn. Lett. 145, 178–186. https://doi.org/10.1016/j.patrec.2021.01.036.

United Nations, 2019. Department of Economic and Social Affairs, Population Division, 2019. World Urbanization Prospects: The 2018 Revision (ST/ESA/SER.A/421). United Nations, New York.

Van Doninck, J., 2016. solarPos: solar position algorithm for solar radiation applications. In: R package version 1.0. https://CRAN.R-project.org/package=solarPos.

Vartholomaios, A., 2019. A machine learning approach to modelling solar irradiation of urban and terrain 3D models. Comput. Environ. Urban. Syst. 78, 101387 https://doi.org/10.1016/j.compenvurbsys.2019.101387.

VDI, 1994. Environmental meteorology, interactions between atmosphere and surface; calculation of short-and long wave radiation. In: Part I: Climate, VDI 3789, Part 2: VDI/DIN- Handbuch Reinhaltung der Luft, Band 1b, Düsseldorf.

VDI, 2008. Environmental meteorology, methods for the human biometeorological evaluation of climate and air quality for urban and regional planning at regional level. In: Part I: Climate, VDI 3787, Part 2: VDI/DIN- Handbuch Reinhaltung der Luft, Band 1b, Düsseldorf.

Wallenberg, N., Lindberg, F., Holmer, B., Thorsson, S., 2020. The influence of anisotropic diffuse shortwave radiation on mean radiant temperature in outdoor urban environments. Urban Clim. 31, 100589 https://doi.org/10.1016/j.uclim.2020.100589.

Watts, N., Amann, M., Arnell, N., Ayeb-Karlsson, S., Beagley, J., Belesova, K., Boykoff, M., Byass, P., Cai, W., Campbell-Lendrum, D., Capstick, S., Chambers, J., Coleman, S., Dalin, C., Daly, M., Dasandi, N., Dasgupta, S., Davies, M., Di Napoli, C., Dominguez-Salas, P., Drummond, P., Dubrow, R., Ebi, K.L., Eckelman, M., Ekins, P., Escobar, L.E., Georgeson, L., Golder, S., Grace, D., Graham, H., Haggar, P., Hamilton, I., Hartinger, S., Hess, J., Hsu, S.-C., Hughes, N., Jankin Mikhaylov, S., Jimenez, M.P., Kelman, I., Kennard, H., Kiesewetter, G., Kinney, P.L., Kjellstrom, T., Kniveton, D., Lampard, P., Lemke, B., Liu, Y., Liu, Z., Lott, M., Lowe, R., Martinez-Urtaza, J., Maslin, M., McAllister, L., McGushin, A., McMichael, C., Milner, J., Moradi-Lakeh, M., Morrissey, K., Munzert, S., Murray, K.A., Neville, T., Nilsson, M., Sewe, M.O., Oreszczyn, T., Otto, M., Owfi, F., Pearman, O., Pencheon, D., Quinn, R., Rabbaniha, M., Robinson, E., Rocklöv, J., Romanello, M., Semenza, J.C., Sherman, J., Shi, L., Springmann, M., Tabatabaei, M., Taylor, J., Triñanes, J., Shumake-Guillemot, J., Vu, B., Wilkinson, P., Winning, M., Gong, P., Montgomery, H., Costello, A., 2021. The 2020 report of the lancet countdown on health and climate change: responding to converging crises. Lancet 397, 129–170. https://doi.org/10.1016/S0140-6736(20)32290-X.

Weyn, J.A., Durran, D.R., Caruana, R., 2019. Can machines learn to predict weather? Using deep learning to predict gridded 500-hPa Geopotential height from historical weather data. J. Adv. Model. Earth Syst. 11, 2680–2693. https://doi.org/10.1029/2019MS001705.

Weyn, J.A., Durran, D.R., Caruana, R., 2020. Improving data-driven global weather prediction using deep convolutional neural networks on a cubed sphere. J. Adv. Model. Earth Syst. 12, e2020MS002109 https://doi.org/10.1029/2020MS002109.

Xie, Y., Ishida, Y., Hu, J., Mochida, A., 2022. A backpropagation neural network improved by a genetic algorithm for predicting the mean radiant temperature around buildings within the long-term period of the near future. Build. Simul. 15, 473–492. https://doi.org/10.1007/s12273-021-0823-6.

Zhang, Z., Dong, Y., 2020. Temperature forecasting via convolutional recurrent neural networks based on time-series data. Complexity 2020, 3536572. https://doi.org/10.1155/2020/3536572.